This item is the archived peer-reviewed author-version of:

Detection of two-dimensional small polarons at oxide interfaces by optical spectroscopy

Detection of two-dimensional small polarons at oxide interfaces by optical spectroscopy

Chi Sin Tang,[1,2,3] Shengwei Zeng,[4] Jing Wu,[3] Shunfeng Chen,[1] Muhammad A. Naradipa,[4] Dongsheng Song,[5] M. V. Milošević[6], Ping Yang,[2] Caozheng Diao,[2] Jun Zhou,[3] Stephen J. Pennycook,[7,9] Mark B.H. Breese,[2,4] Chuanbing Cai,[1] Thirumalai Venkatesan,[10] Ariando Ariando,[4] Ming Yang,[8,*] Andrew T.S. Wee,[4,9,*] Xinmao Yin [1,*]

Affiliations:

[1]Shanghai Key Laboratory of High Temperature Superconductors, Department of Physics, Shanghai University, Shanghai 200444, China

[2]Singapore Synchrotron Light Source (SSLS), National University of Singapore, Singapore 117603

[3]Institute of Materials Research and Engineering, A∗STAR (Agency for Science, Technology and Research), 2 Fusionopolis Way, Singapore, 138634 Singapore

[4]Department of Physics, Faculty of Science, National University of Singapore, Singapore 117542

[5]Institute of Physical Science and Information Technology, Anhui University, Hefei 230601, China

[6]Departement Fysica, Universiteit Antwerpen, Groenenborgerlaan 171, B-2020 Antwerpen, Belgium

[7]Department of Materials Science and Engineering, National University of Singapore, Singapore, 117575, Singapore

[8]Department of Applied Physics, The Hong Kong Polytechnic University, Kowloon, Hong Kong, China

[9]Centre for Advanced 2D Materials and Graphene Research, National University of Singapore, Singapore 117546

[10]Center for Quantum Research and Technology, University of Oklahoma, Norman, Oklahoma 73019, USA

*Correspondence to: kevin.m.yang@polyu.edu.hk (M.Y.), phyweets@nus.edu.sg (A.T.S.W)，yinxinmao@shu.edu.cn (X.Y.)

Two-dimensional (2D) perovskite oxide interfaces are ideal systems to uncover diverse emergent properties such as the arising polaronic properties from short-range charge-lattice interactions. Thus, a technique to detect this quasiparticle phenomena at the buried interface is highly coveted. Here, we report the observation of 2D small-polarons at the $LaAlO_3$/$SrTiO_3$ (LAO/STO) conducting interface using high-resolution spectroscopic ellipsometry. First-principles investigations shows that interfacial electron-lattice coupling mediated by the longitudinal phonon mode facilitates the formation of these polarons. This study resolves the longstanding question by attributing the formation of interfacial 2D small polarons to the significant mismatch between experimentally measured interfacial carrier density and theoretical values. Our study sheds light on the complexity of broken periodic lattice-induced quasi-particle effects and its relationship with exotic phenomena at complex oxide interfaces. Meanwhile, this work establishes spectroscopic ellipsometry as a useful technique to detect and locate optical evidence of polaronic states and other emerging quantum properties at the buried interface.

Introduction

The emergence of quasiparticles due to the interplay between electronic and lattice degrees of freedom in strongly-correlated systems is the cornerstone of multiple fundamental phenomena including transport processes, colossal magnetoresistance[1] and high-temperature superconductivity[2]. Polarons are an ideal example where motion of mobile charges are retarded due to strong charge-lattice interaction [3]. Though well-established in 3D systems[4], polaronic formation and modifications to their properties by reduced dimensionality in 2D systems remains challenging due to the incomplete understanding of polaron self-trapping in anisotropic structures[5]. Nevertheless, the key role of strongly-bound electronic polarons and bipolarons which possess lower-temperature coherence could hold the key in understanding many-body phenomena such as itinerant ferromagnetism[6] and unconventional Cooper pairing in superconductivity[7, 8]. Such prospects are tantalizingly attractive especially with reports of 2D polaronic behaviour[4, 5] alongside their causality with 2D superconductivity[9]. The effective identification of polaronic activities and the underlying mechanisms leading to their formation play a critical role in assessing the distinguish the short- and long-range transport characteristics and sheds new light on the nature of quasiparticle interactions in diverse material systems[4]. Such knowledge holds immediate relevance especially in the functionalization of novel quantum systems in applications over a wide range of domains related to electronic transport[10, 11], photocatalysis[12] and energy storage devices[13].

Recent reports of 2D perovskite oxide superconductivity at the $LaAlO_3/KTaO_3$ interface have renewed fresh interests in the emergence of anomalous quantum metallic states[14, 15]. The quintessential $LaAlO_3/SrTiO_3$ (LAO/STO) conducting interface remains the ideal candidate for such investigation especially with the versatility and capacity to effectively manipulate its charge, spin, lattice, and orbital degrees-of-freedom at the nanometer-thickness interface[16]. Furthermore, insights to the interfacial many-body charge dynamics in the region ~10 meV within the Fermi level is pivotal to explain the severe discrepancy between the theoretically predicted 0.5 electrons per unit cell (e^-/uc) charge transfer by multiple models[10, 17, 18], as compared to a meagre 0.05 e^-/uc elucidated by experiments[19-21].

Here, we make the observation of small-polarons at the LAO/STO interface using high-resolution spectroscopic ellipsometry, a highly sensitive non-destructive photon-in photon-out optical technique with a spectral resolution of 0.02 eV which, with its full polarization and symmetry features, can explore the role of electron-phonon coupling and effectively resolve

the anisotropic properties of the LAO/STO system and extract the optical properties of its interfacial 2D electron gas. This is in light of the progress in the experimental techniques to characterize polaronic responses, that while there were initially no evidence of sufficiently large electron-phonon coupling to induce small polaron formation in Nb-doped STO[22], a subsequent experimental study then suggested polaronic correlations in the LAO/STO system which possesses strongly frequency-dependent mobility similar to that of Nb-doped STO[23]. Even though significant breakthrough was then made with the observation of large polaron at the LAO/STO interface using angle resolved photoemission spectroscopy (ARPES)[10], it can only study the interfacial properties in the vicinity of the fermi level. The unique properties of spectroscopic ellipsometry allows one to study the electronic properties and quasiparticle dynamics of systems into the near infrared, visible and ultraviolet regime[24-27] that provide evidence in identifying the optical response of the small polarons presented at the 2D LAO/STO interface. First-principles calculations further suggest the strong coupling between the interfacial electrons and the Ti-lattice as the key mechanism leading to the formation of the localized small polarons which is 2D in nature. Based on an integrated analysis of our experimental results and findings from the first-principle studies, the hard longitudinal optical phonon mode, LO3, which has previously been identified as the key mediator in the formation of large polarons[10, 13], has also been determined to play a critical role in the formation of the 2D small-polarons. Importantly, by showing that ~50% of the interfacial charges couple strongly with the Ti lattice sites to form highly localized 2D small polarons [Fig. 1(a)], this study effectively resolved the longstanding question why the experimentally-measured interfacial carrier density is significantly lower than theoretically predicted values[10, 17, 18]. In light of how quasiparticle dynamics governs superconductivity at perovskite oxide interfaces, our study further highlights the strong interactions between excess interfacial electrons and Ti lattices that results in the polaronic states where lattice distortion invariably breaks the periodic lattice symmetry[4]. This study is therefore potentially analogous to other heterostructure systems such as that of magic-angle twisted bilayer graphene where their superconductive states could be attributed to the many-body correlations induced by broken periodic lattice symmetry[28-32]. With the escalating challenge to characterize emergent quantum orders in complex low-dimensional systems, this study further highlights spectroscopic ellipsometry as the premier experimental methodology to unambiguously identify and analyse anisotropic quasiparticle dynamics and other emergent order-parameter nanostructures at the buried complex quantum interfaces.

Results

Sample Synthesis and Characterization

Three high-quality single crystalline 8 u.c. LaAlO$_3$/SrTiO$_3$ labelled *N1*-LAO/STO, *N2*-LAO/STO, and *N3*-LAO/STO, respectively, are synthesized with increasing degree of oxygen vacancies, thereby resulting in different carrier concentrations – 9.4×10^{12} cm^{-2} (*N1*-LAO/STO), 1.0×10^{14} cm^{-2} (*N2*-LAO/STO), and 4.5×10^{16} cm^{-2} (*N3*-LAO/STO) [Fig. S1] (details in Section I.B, supplementary material) as further confirmed based on synchrotron-based X-ray absorption spectroscopy [Fig. 1] (details in Section I.B, supplementary material). The quality of the LAO/STO interfaces has been confirmed using a series of experimental techniques including atomic force microscopy (AFM) [Fig. 1(a)], high angle annular dark field STEM (HAADF–STEM) [Fig. 1(b)] and high-resolution X-ray diffraction [Figs. S2–S4] which suggest atomically flat terrace structures, high-quality morphology, and crystallinity.

Temperature-dependent Spectroscopic Ellipsometry

Temperature-dependent optical characterization of *N1*-LAO/STO is performed using Spectroscopic Ellipsometry with the complex dielectric function, $\varepsilon(\omega)=\varepsilon_1(\omega)+i\varepsilon_2(\omega)$ [Fig. 2(a)] (details in Section II.D, supplementary material). The fitted results of both the ε_1 and ε_2 spectra show Kramers-Kronig consistency and they are in good agreement with previous experimental studies in regions above 1 eV[33]. The optical features in the photon energy region of ~2–3 eV are likely the result of interband transitions. As seen thereafter in the electronic band structure [Fig. 4(g)], the feature at ~3.0 eV can be ascribed to the valence to conduction band edge transition while the features in between 2—3 eV are likely due to optical transitions between the valence band and polaron band (to be discussed thereafter). The Drude response below 1 eV suggests that it is a conducting system ascribed to the interfacial 2D delocalized electrons. Interestingly, a previously unidentified prominent mid-gap peak feature is observed in the near-infrared regime at ~0.66 eV (annotated by arrow) throughout all temperature which has not been observed or scrutinized previously. With the repeated characterization of similar LAO/STO interface synthesized under the same experimental conditions, this feature persists. Thus, confirming that this is not an optical artefact that arises from the optical measurements. Besides, with the focus of this study on the optical features in the near-IR photon energy region, it allows for the detailed scrutiny to account for the origin of this previously unaccounted for optical feature. With minimal oxygen defect from *N1*-LAO/STO and having previously confirmed the high-quality and crystallinity of the sample, one can rule out the contribution of

oxygen vacancies and defects states (Discussion eliminating other factors to be discussed thereafter). Instead, it bears resemblance to the optical absorption feature of small polaron due to its asymmetry[34]. As discussed in greater detail thereafter, this feature is attributed to the interfacial 2D small polarons.

The ε_2 spectra of N1-LAO/STO is further converted to optical conductivity, σ_1, using Supplementary Equation 11 (details in Section III.A. supplementary material) for further polaron analysis [Fig. 2(b)]. While the previously observed Drude response falls below the spectral range, the polaron peak remains prominent at ~0.82–0.98 eV where its asymmetric shape characteristic of small polaron remains[34]. The prominent nature of this optical peak clearly indicates that it is a standalone optical feature independent of any other features present in the optical spectra. Since the small polarons optical features arise due to electron hopping between in-plane neighbouring Ti-sites upon activation, the peaks can thus be modelled using the Bryksin small-polaron model to analyze its temperature-dependent properties[35]. Specifically, parameters including the polaron hopping energy, E_a, bandwidth, Γ, and phonon energy, E_{LO}, can be derived (details in Section III.A, supplementary material).

The optical polaron responses is very compatible with the theoretical Bryksin small-polaron model for both N1- and N2-LAO/STO interfaces, respectively, throughout the entire temperature range as seen in the zoom in stacked σ_1 spectra in [Figs. 2(c) and 2(f)] (further temperature-dependent analyses to be discussed in Fig. S3 and Section III.B, supplementary material). This indicates that the near-infrared responses in both N1- and N2-LAO/STO interfaces are of small-polaron origin. Besides, they are notably distinct from the previously identified interfacial large polarons[10] as confirmed in the computational studies presented thereafter.

We analyze the temperature-dependent ε_1 and ε_2 spectra, respectively, of N2-LAO/STO [Fig. 2(d)] to investigate how increasing interfacial carrier concentration affects the modifies the polaronic response. Once again, while the optical spectra of both the N1- and N2-LAO/STO interfaces are Kramers-Kronig consistent and display similar optical features with previous reports[33], the Drude response for N2-LAO/STO due to higher interfacial carrier concentration. Notably, the mid-gap previously attributed to the small polaron response persists at the N2-LAO/STO interface across all temperature at a redshifted position of ~0.42 eV. Similar to the previously characterized N1-LAO/STO, this optical feature persists present for other

synthesized LAO/STO interfaces possessing the same conditions as N2-LAO/STO. thereby confirming once again that this is not a mere optical artefact. Related to the polaron activation energy E_a, this redshift in the polaron peak is consistent with our theoretical study where LAO/STO interfaces with higher interfacial charge concentration tend to have a lower E_a, as discussed in greater detail thereafter. Based on the Bryksin analysis (Section III.A, supplementary material), while the Drude response is red-shifted below the spectral range, the polaron peak remains prominent [Fig. 2(e)] and they display high consistency between the experimental results and theoretical fitting throughout the entire measured temperature range as seen in the temperature-dependent stacked σ_1 spectra belonging to $N2$-LAO/STO in [Fig. 2(f)] where the polaron activation energy, E_a, is significantly lower (Fig. S3 and Section III.B, supplementary material).

Compared to $N1$ and $N2$-LAO/STO, $N3$-LAO/STO shows a marked increase in temperature-dependence especially for the ε_1 spectra while the ε_2 spectra undergoes a significant change in the low-energy region where the previously observed near-infrared polaron peak is further redshifted to photon energy below the instrument spectral limit [Fig. 3(a)]. Hence, analysis of the small polaron response will be restricted to the $N1$- and $N2$-LAO/STO interfaces (details in Section III.B, supplementary material).

Analyzing the Small Polaron Parameters

Using Supplementary equation 9b in the supplementary material to perform curve fitting for the respective σ_1 spectra in the photon energy region where the polaron peak is located (stacked σ_1 spectra of both $N1$- and $N2$-LAO/STO interfaces displayed in Figs. 2(c) and 2(f), respectively), the hopping energy, E_a, polaron band width, Γ, and phonon energy, E_{LO}, as displayed in Figs. 3(b)–3(d) respectively, of the 2D interfacial polarons at the $N1$- and $N2$-LAO/STO interfaces are elucidated. E_a of $N2$-LAO/STO falls significantly lower to the region between ~0.11—0.12 eV compared to $N1$-LAO/STO's ~0.24—0.25 eV. Between 77 and 300K, temperature-dependence of E_a of both $N1$- and $N2$-LAO/STO follows similar trend with a slight but apparent increase with rising temperature as it becomes easier for the electron to move from one Ti-site to the next[34]. The distinct reduction in E_a of $N2$-LAO/STO compared to $N1$-LAO/STO may be partially attributed to the increase in overlapping potential wells due to higher oxygen vacancies at the interface that allows for a greater ease of interstitial charge hopping. As scrutinized in greater detail thereafter, theoretical calculations quantitively show that the polaron state of the LAO/STO interface with higher 2D excess electrons is formed at

an energy position nearer to the conduction band edge along the Γ-point of the band structure. This quantitively accounts for why the polaron activation energy, E_a, for the more conducting $N2$-LAO/STO is lower than that of $N1$-LAO/STO which possesses lower interfacial charge concentration (see [Fig. 4(g)]). Comparison of E_a between $N1$-LAO/STO and $N2$-LAO/STO further suggests that an increase in interfacial charge density has a greater influence on the interfacial polarons than temperature.

The polaron bandwidth, Γ, of $N2$-LAO/STO is slightly larger than $N1$-LAO/STO [Fig. 3(c)]. Nevertheless, both display similar temperature-dependent trends with a monotonic width broadening from ~0.039 to ~0.057 eV for $N2$-LAO/STO and relatively smaller increase of ~0.019 to ~0.026 eV for $N1$-LAO/STO. This progressive broadening with rising temperature is consistent with the behaviour of small-polarons which corresponds with the phonon broadening of the local electronic energy levels which in turn progressively broadens these absorption bands[34]. To account for the relatively larger bandwidth belonging to $N2$-LAO/STO as compared to $N1$-LAO/STO, it is first noted that the conduction band of the LAO/STO interface is mainly dominated by multiple overlapping bands belonging to the Ti d-orbitals (compare conduction band states of the Ti and O orbitals based on PDOS calculations in Figs. 4(e) and 4(f), respectively). With an increase in the charge concentration at the LAO/STO interface through the introduction of oxygen vacancies, there will invariably be an increase in the number of conduction band states that will be occupied when polaron transitions take place. As a result, one will expect an increase in the distribution of polaron energy as evidenced by the broadening of the polaron bandwidth, Γ, as observed in our experimental result[35, 36].

Role of LO3 in the Formation of the Interfacial Small Polarons

Finally, the E_{LO} of both $N1$- and $N2$-LAO/STO does not have any clear temperature trend [Fig. 3(b)] but their values fluctuate between ~0.102–0.106 eV for $N1$-LAO/STO and ~0.13–0.18 eV for $N2$-LAO/STO. These values are consistent with the hard longitudinal optical phonon, LO3. This phonon mode is attributed to the atomic displacements leading to the breathing distortion of an octahedral cage that surrounds a Ti-site[10]. The role that LO3 plays in mediating electron-phonon coupling is not only restricted to the LAO/STO interface, but also on the surfaces and within the bulk of STO substrates[22, 37-39]. In the case of the LAO/STO interfacial polaron reported in this study, it is consistent with previous studies where there are barely any changes in energy position with temperature[10, 40]. Moreover, as the LO3 phonon falls within the energy range of ~100 meV where our interfacial small polaron are detected, it is the most

probable phonon mode that mediates the formation of the interfacial small polarons observed in our study. Besides, as it possesses the highest electron-phonon coupling constant amongst the LO-modes[40-43], it allows for the formation of small polarons particularly facilitated by short-range electron-phonon interaction. The presence of LO3 phonon mode plays an important role in controlling the 2D interfacial carrier mobility[10]. Considering the role that LO3 plays in the interfacial polaron formation, the larger E_{LO} magnitude for $N2$-LAO/STO may be attributed to structural changes due to electrostatic doping by the increase in oxygen vacancies[44] or possible weaker coupling to additional phonon modes. To further account for the slight discrepancies between the theoretical energy position of the LO3 phonon (at ~100 meV)[10] and that which is derived from our data fitting, interfacial electric field, phonon coupling across the LAO/STO interface, propagation lattice distortion across the interface may be likely factors leading to such quantitative differences[45]. Nevertheless, the phonon mode analysis provided in this study and the preceding ones highlights the critical role that electron-phonon interaction plays in the formation of this 2D interfacial polaron. The identification of E_{LO} as the energy position of LO3 phonons is a clear indication of polarons and the identification of polaronic effects[46, 47] while distinguish it from other phenomena. Besides, while the large polarons in LAO/STO have been attributed to the LO3 phonons[10], this analysis conclusively shows that the LO3 phonons also plays the direct role in the formation of the small polarons at the LAO/STO interface.

Overall, the compatibility between the optical features in the respective σ_1 spectra and the Bryksin small-polaron model alongside the considerably reasonable fitting error (as denoted by the error bars) are indications that these optical responses are indeed signatures of small polaron present at the LAO/STO interface. Besides, the general temperature-dependent trends and asymmetric peak feature of both $N1$- and $N2$-LAO/STO provide further indications of the small polaron dynamics at the LAO/STO interfaces[35]. The temperature-dependent behaviours also allow us to rule out the contribution of large polaron to these optical features[34]. The use of the Bryksin model to verify the small interfacial behaviour at the LAO/STO interface is further confirmed and substantiated via first-principles study as discussed thereafter.

Further Eliminating other Possible Contributing Factors to the Optical Responses

Besides ruling out the possibility of defect states contributing to the formation of the near-infrared optical response, we rule out any other possible factors that may lead to the optical features in Fig. 2. The presence of exciton may be omitted because while exciton weakens

significantly with rising temperature[48, 49], the near-IR feature detected at the LAO/STO interface has a trend contrary to that of exciton with an intensity increase with temperature.

With the vanishingly small ferromagnetic response contributed by the LAO/STO interface[50], the onset of magnons can also be omitted. Finally, any contribution by plasmon excitation can also be ruled out due to detection of plasmon requires the simultaneous presence of a zero-crossing in the ε_1 spectrum alongside a prominent peak feature in the Loss-function spectrum which are not present in the respective components of the dielectric functions[26, 51].

Therefore, by eliminating these possible contributing factors, the polaronic origin of these mid-IR peaks at the LAO/STO interface can be safely concluded.

First-principles Calculations Elucidating Small Polaron Properties

Extensive first-principles studies are conducted to further substantiate our experimental findings on how excess electrons interact with the interfacial Ti ions to form small polarons and account for the missing interfacial electrons. The LAO/STO interface was modelled using a $(LaAlO_3)_{6.5}/(SrTiO_3)_{8.5}$ superlattice [Fig. 4(a)] (details in Section V, supplementary material) with 0.5 e^-/uc charge transfer from the LAO layer to the interface. Previous studies have shown that this modelized structure has been widely used to mimic and simulate the LAO/STO interfacial effects[52-55]. Hence, the results yielded by the current study provide important insights to the phenomena observed in real experimental systems. Besides, the polaron formation energy at this charge-transfer density is ~160 meV lower than the non-polaron state [Fig. S8] (details in Section V.B, supplementary material). The interfacial polaron states are therefore more stable than the free-electron states. While charge transfer from the LAO layer penetrates the interface into the STO layer and localize at the Ti lattice sites (blue superimposed partial charge density in the STO layer in [Fig. 4(b)], it is only at the interfacial Ti lattice sites that the localized charge concentration is sufficiently large to form small polarons [Fig. 4(a)]. Small polaron formation is further evidenced by a slight elongation of the in-plane Ti-O bonds by about +0.08 Å relative to Ti-sites where there are no polaron states as seen in the interfacial lattice cross-section [Fig. 4(c)]. This is consistent with the magnitude of lattice deformation due to small polaron formation as reported in other systems such as TiO_2 and Nb-doped STO[56-58]. Moreover, as noticed in the top view of interfacial structure superimposed with the partial charge density of the polaron state [Fig. 4(d)], the electron density only localizes at the distorted Ti site and not homogeneously at the others. With the concurrent presence of local lattice deformation as seen in the Ti-O elongation [Fig. 4(c)] and the onset of localized electron

density at the affected Ti-lattice sites [Fig. 4(d)], these are clear fingerprints of the formation of small polarons[56]. Collectively, these are evidence of small polaron states with *two-dimensional* character.

The 2D small polarons is further confirmed by the projected density of states (PDOS) at the interfacial TiO_2-sublayer. [Fig. 4(e)] shows that strong charge-lattice interaction causes a split in the in-plane Ti-d_{xy} states from the conduction band edge and forms an isolated mid-gap state – another distinctive hallmark of the polaron state – which hybridizes weakly with the nearest in-plane O-p_y/p_y states [Fig. 4(f)]. This is yet another signature of a polaron state with two-dimensional feature due to the in-plane hybridized orbitals - consistent with the prominent in-plane Ti-O bond elongation alongside the in-plane polaron charge density distribution state [Figs. 4(a)—4(d)]. Therefore, it can be concluded to be an interfacial *two-dimensional* small polaron. By further modelling the partial charge density for the polaronic band in the energy range between -1 and -2 eV, the integration of the partial charge density leads a value of 0.25 e^-/uc – half of the total transferred electron of 0.5 e^-/uc. Hence, we deduced that about half of the electrons interact with the interfacial Ti lattice to form the polaron state [Fig. 4(a)] where it is further confirmed by a previous study[10].

In tandem with the experimental study involving LAO/STO interfaces with different charge concentrations, a less conducting LAO/STO interface with 0.4 e^-/uc charge transfer is modelled. While its polaron stability is reduced, the interfacial polaron state remains favourable with an energy of 126 meV lower than the non-polaron state [Fig. S8] (details in Section V.B, supplementary material) due to decreased electron-electron repulsion that weakens the excess electrons interaction and the Ti lattice sites[56].

The reduction in carrier density also has strong influence on the electronic properties of the LAO/STO interface with the polaron. Fig. 4(g) compares the band structures of the LAO/STO interfaces with 0.5 e^-/uc (black solid lines) and 0.4 e^-/uc charge transfer (red dashed lines), respectively. With the conduction band edge of both interfaces aligned at -0.365 eV indicated by the overlapping black and red bands at the Γ-point, the polaron state for the less conducting system is located ~0.15 eV *lower* than the more conducting interface – denoted by yellow shaded region in [Fig. 4(g)]. This is consistent with the experimental results that compares *N1*-LAO/STO which has a lower interfacial charge concentration than *N2*-LAO/STO [Figs. 2(b) and 2(e), respectively]. The polaron positions – directly related to the polaron activation energy, E_a – of the more conducting *N2*-LAO/STO is lower compared to *N1*-LAO/STO [Fig. 3(b)].

This also explains why the polaron position falls below the instrument spectral range for *N3*-LAO/STO.

Discussion and Conclusion

The combination of experimental results and theoretical calculations provides clear evidence of the onset of 2D small polarons at the LAO/STO interface. This study is important in understanding how quasiparticle dynamics governs superconductivity at perovskite oxides heterointerfaces and is potentially analogous to other heterostructure systems especially in twisted bilayer graphene[30, 59]. The strong interactions between excess interfacial electrons and Ti lattices result in the polaronic states where lattice distortion invariably breaks the periodic lattice symmetry[4, 60]. Meanwhile, our calculations show that the formation of small polarons due to considerable loss in electron kinetic energy. This in turn leads to in a significant reduction in polaron bandwidth to ~0.5 eV compared to ~1.2 eV for free electron states. This band flattening strengthens the electron-electron correlations and is key to the emergence of the interfacial superconductivity[61]. This superconductive mechanism in perovskite oxide interfaces resembles the superconductive properties in magic-angle twisted bilayer graphene with an interlayer misalignment of 1.1°[29, 30]. Specifically, flat electronic bands are present at certain interlayer twist angles[29, 30]. The formation of the Moiré patterns breaks the original periodic structure, and the inhomogeneity of the electron systems drastically reduces the Fermi velocity. This significantly modifies the electronic properties where flat bands are form at the Fermi level which, in turn, leads to superconductivity[62]. Similar to the interfacial superconductivity of oxide heterostructures, the emergence of strong electron-electron correlations because of broken periodic lattice symmetry holds the key to the onset of superconductivity in magic angle twisted bilayer graphene[28] (details in Section VI, supplementary material).

The formation of 2D small polaron at the LAO/STO interface has led to the localization of 50% of the interfacial excess electrons. Notably, the interfacial electron density and lattice distortion are pivotal in dictating the small polaron dynamics and it holds important implications on how quasiparticle dynamics mediates superconductivity in complex heterointerfaces including perovskite oxides and magic-angle twisted bilayer graphene. It further highlights spectroscopic ellipsometry as the ideal experimental technique to unambiguously identify and characterize anisotropic quasiparticle dynamics and other emergent order-parameter nanostructures at the buried complex quantum interfaces and other low-dimensional heterostructure systems.

References:

1.	N. Mannella, W. L. Yang, X. J. Zhou, H. Zheng, J. F. Mitchell, J. Zaanen, T. P. Devereaux, N. Nagaosa, Z. Hussain and Z. X. Shen, Nature **438** (7067), 474-478 (2005).
2.	P. A. Lee, N. Nagaosa and X.-G. Wen, Reviews of Modern Physics **78** (1), 17-85 (2006).
3.	T. Holstein, Annals of Physics **8** (3), 343-389 (1959).
4.	C. Franchini, M. Reticcioli, M. Setvin and U. Diebold, Nature Reviews Materials **6** (7), 560-586 (2021).
5.	K. P. McKenna, M. J. Wolf, A. L. Shluger, S. Lany and A. Zunger, Physical Review Letters **108** (11), 116403 (2012).
6.	G. Valtolina, F. Scazza, A. Amico, A. Burchianti, A. Recati, T. Enss, M. Inguscio, M. Zaccanti and G. Roati, Nature Physics **13** (7), 704-709 (2017).
7.	M. Danilov, E. G. C. P. van Loon, S. Brener, S. Iskakov, M. I. Katsnelson and A. I. Lichtenstein, npj Quantum Materials **7** (1), 50 (2022).
8.	K. Jin, N. P. Butch, K. Kirshenbaum, J. Paglione and R. L. Greene, Nature **476** (7358), 73-75 (2011).
9.	M. Kang, S. W. Jung, W. J. Shin, Y. Sohn, S. H. Ryu, T. K. Kim, M. Hoesch and K. S. Kim, Nature Materials **17** (8), 676-680 (2018).
10.	C. Cancellieri, A. S. Mishchenko, U. Aschauer, A. Filippetti, C. Faber, O. S. Barišić, V. A. Rogalev, T. Schmitt, N. Nagaosa and V. N. Strocov, Nature Communications **7** (1), 10386 (2016).
11.	J. C. Garcia, M. Nolan and N. A. Deskins, The Journal of Chemical Physics **142** (2), 024708 (2015).
12.	D. Ghosh, E. Welch, A. J. Neukirch, A. Zakhidov and S. Tretiak, The Journal of Physical Chemistry Letters **11** (9), 3271-3286 (2020).
13.	W. Zheng, B. Sun, D. Li, S. M. Gali, H. Zhang, S. Fu, L. Di Virgilio, Z. Li, S. Yang, S. Zhou, D. Beljonne, M. Yu, X. Feng, H. I. Wang and M. Bonn, Nature Physics **18** (5), 544-550 (2022).
14.	C. Liu, X. Yan, D. Jin, Y. Ma, H.-W. Hsiao, Y. Lin, M. Bretz-Sullivan Terence, X. Zhou, J. Pearson, B. Fisher, J. S. Jiang, W. Han, J.-M. Zuo, J. Wen, D. Fong Dillon, J. Sun, H. Zhou and A. Bhattacharya, Science **371** (6530), 716-721 (2021).

15.   Z. Chen, Y. Liu, H. Zhang, Z. Liu, H. Tian, Y. Sun, M. Zhang, Y. Zhou, J. Sun and Y. Xie, Science **372** (6543), 721-724 (2021).

16.   H. Y. Hwang, Y. Iwasa, M. Kawasaki, B. Keimer, N. Nagaosa and Y. Tokura, Nature Materials **11** (2), 103-113 (2012).

17.   N. Nakagawa, H. Y. Hwang and D. A. Muller, Nature Materials **5** (3), 204-209 (2006).

18.   L. Yu and A. Zunger, Nature Communications **5** (1), 5118 (2014).

19.   S. Thiel, G. Hammerl, A. Schmehl, C. W. Schneider and J. Mannhart, Science **313** (5795), 1942-1945 (2006).

20.   A. Brinkman, M. Huijben, M. van Zalk, J. Huijben, U. Zeitler, J. C. Maan, W. G. van der Wiel, G. Rijnders, D. H. A. Blank and H. Hilgenkamp, Nature Materials **6** (7), 493-496 (2007).

21.   N. Reyren, S. Thiel, A. D. Caviglia, L. F. Kourkoutis, G. Hammerl, C. Richter, C. W. Schneider, T. Kopp, A. S. Rüetschi, D. Jaccard, M. Gabay, D. A. Muller, J. M. Triscone and J. Mannhart, Science **317** (5842), 1196-1199 (2007).

22.   J. L. M. van Mechelen, D. van der Marel, C. Grimaldi, A. B. Kuzmenko, N. P. Armitage, N. Reyren, H. Hagemann and I. I. Mazin, Physical Review Letters **100** (22), 226403 (2008).

23.   A. Dubroka, M. Rössle, K. W. Kim, V. K. Malik, L. Schultz, S. Thiel, C. W. Schneider, J. Mannhart, G. Herranz, O. Copie, M. Bibes, A. Barthélémy and C. Bernhard, Physical Review Letters **104** (15), 156807 (2010).

24.   X. Yin, Q. Wang, L. Cao, C. S. Tang, X. Luo, Y. Zheng, L. M. Wong, S. J. Wang, S. Y. Quek, W. Zhang, A. Rusydi and A. T. S. Wee, Nature Communications **8** (1), 486 (2017).

25.   X. Yin, S. Zeng, T. Das, G. Baskaran, T. C. Asmara, I. Santoso, X. Yu, C. Diao, P. Yang, M. B. H. Breese, T. Venkatesan, H. Lin, Ariando and A. Rusydi, Physical Review Letters **116** (19), 197002 (2016).

26.   X. Yin, C. S. Tang, S. Zeng, T. C. Asmara, P. Yang, M. A. Naradipa, P. E. Trevisanutto, T. Shirakawa, B. H. Kim, S. Yunoki, M. B. H. Breese, T. Venkatesan, A. T. S. Wee, A. Ariando and A. Rusydi, ACS Photonics **6** (12), 3281-3289 (2019).

27.   C. S. Tang, X. Yin, S. Zeng, J. Wu, M. Yang, P. Yang, C. Diao, Y. P. Feng, M. B. H. Breese, E. E. M. Chia, T. Venkatesan, M. Chhowalla, A. Ariando, A. Rusydi and A. T. S. Wee, Advanced Materials **32** (34), 2000153 (2020).

28.   Y. Xie, B. Lian, B. Jäck, X. Liu, C.-L. Chiu, K. Watanabe, T. Taniguchi, B. A. Bernevig and A. Yazdani, Nature **572** (7767), 101-105 (2019).

29.   Y. Cao, V. Fatemi, A. Demir, S. Fang, S. L. Tomarken, J. Y. Luo, J. D. Sanchez-Yamagishi, K. Watanabe, T. Taniguchi, E. Kaxiras, R. C. Ashoori and P. Jarillo-Herrero, Nature **556** (7699), 80-84 (2018).

30.   Y. Cao, V. Fatemi, S. Fang, K. Watanabe, T. Taniguchi, E. Kaxiras and P. Jarillo-Herrero, Nature **556** (7699), 43-50 (2018).

31.   A. G. Swartz, H. Inoue, T. A. Merz, Y. Hikita, S. Raghu, T. P. Devereaux, S. Johnston and H. Y. Hwang, Proceedings of the National Academy of Sciences **115** (7), 1475 (2018).

32.   A. D. Caviglia, S. Gariglio, N. Reyren, D. Jaccard, T. Schneider, M. Gabay, S. Thiel, G. Hammerl, J. Mannhart and J. M. Triscone, Nature **456** (7222), 624-627 (2008).

33.   T. C. Asmara, A. Annadi, I. Santoso, P. K. Gogoi, A. Kotlov, H. M. Omer, M. Motapothula, M. B. H. Breese, M. Rübhausen, T. Venkatesan, Ariando and A. Rusydi, Nature Communications **5** (1), 3663 (2014).

34.   D. Emin, Physical Review B **48** (18), 13691-13702 (1993).

35.   C. A. Triana, C. G. Granqvist and G. A. Niklasson, Journal of Applied Physics **119** (1), 015701 (2016).

36.   C. A. Triana, C. G. Granqvist and G. A. Niklasson, Journal of Applied Physics **118** (2), 024901 (2015).

37.   Y. J. Chang, A. Bostwick, Y. S. Kim, K. Horn and E. Rotenberg, Physical Review B **81** (23), 235109 (2010).

38.   Z. Wang, S. McKeown Walker, A. Tamai, Y. Wang, Z. Ristic, F. Y. Bruno, A. de la Torre, S. Riccò, N. C. Plumb, M. Shi, P. Hlawenka, J. Sánchez-Barriga, A. Varykhalov, T. K. Kim, M. Hoesch, P. D. C. King,

W. Meevasana, U. Diebold, J. Mesot, B. Moritz, T. P. Devereaux, M. Radovic and F. Baumberger, Nature Materials **15** (8), 835-839 (2016).

39.   C. Chen, J. Avila, E. Frantzeskakis, A. Levy and M. C. Asensio, Nature Communications **6** (1), 8585 (2015).

40.   W. Meevasana, X. J. Zhou, B. Moritz, C. C. Chen, R. H. He, S. I. Fujimori, D. H. Lu, S. K. Mo, R. G. Moore, F. Baumberger, T. P. Devereaux, D. van der Marel, N. Nagaosa, J. Zaanen and Z. X. Shen, New Journal of Physics **12** (2), 023004 (2010).

41.   G. Verbist, F. M. Peeters and J. T. Devreese, Ferroelectrics **130** (1), 27-34 (1992).

42.   N. Choudhury, E. J. Walter, A. I. Kolesnikov and C.-K. Loong, Physical Review B **77** (13), 134111 (2008).

43.   M. Cardona, Physical Review **140** (2A), A651-A655 (1965).

44.   D. Doennig and R. Pentcheva, Scientific Reports **5** (1), 7909 (2015).

45.   C. L. Jia, S. B. Mi, M. Faley, U. Poppe, J. Schubert and K. Urban, Physical Review B **79** (8), 081405 (2009).

46.   V. N. Strocov, C. Cancellieri and A. S. Mishchenko, in *Spectroscopy of Complex Oxide Interfaces: Photoemission and Related Spectroscopies*, edited by C. Cancellieri and V. N. Strocov (Springer International Publishing, Cham, 2018), pp. 107-151.

47.   C. Verdi, F. Caruso and F. Giustino, Nature Communications **8** (1), 15769 (2017).

48.   F. Cadiz, E. Courtade, C. Robert, G. Wang, Y. Shen, H. Cai, T. Taniguchi, K. Watanabe, H. Carrere, D. Lagarde, M. Manca, T. Amand, P. Renucci, S. Tongay, X. Marie and B. Urbaszek, Physical Review X **7** (2), 021026 (2017).

49.   K. He, N. Kumar, L. Zhao, Z. Wang, K. F. Mak, H. Zhao and J. Shan, Physical Review Letters **113** (2), 026803 (2014).

50.   A. Fête, S. Gariglio, C. Berthod, D. Li, D. Stornaiuolo, M. Gabay and J. M. Triscone, New Journal of Physics **16** (11), 112002 (2014).

51.   D. Pines, Reviews of Modern Physics **28** (3), 184-198 (1956).

52.   R. Pentcheva and W. E. Pickett, Physical Review Letters **102** (10), 107602 (2009).

53.   Z. Zhong and P. J. Kelly, Europhysics Letters **84** (2), 27001 (2008).

54.   Z. S. Popović, S. Satpathy and R. M. Martin, Physical Review Letters **101** (25), 256801 (2008).

55.   H. Banerjee, S. Banerjee, M. Randeria and T. Saha-Dasgupta, Scientific Reports **5** (1), 18647 (2015).

56.   X. Hao, Z. Wang, M. Schmid, U. Diebold and C. Franchini, Physical Review B **91** (8), 085204 (2015).

57.   N. A. Deskins and M. Dupuis, Physical Review B **75** (19), 195212 (2007).

58.   M. Setvin, C. Franchini, X. Hao, M. Schmid, A. Janotti, M. Kaltak, C. G. Van de Walle, G. Kresse and U. Diebold, Physical Review Letters **113** (8), 086402 (2014).

59.   X. Lu, P. Stepanov, W. Yang, M. Xie, M. A. Aamir, I. Das, C. Urgell, K. Watanabe, T. Taniguchi, G. Zhang, A. Bachtold, A. H. MacDonald and D. K. Efetov, Nature **574** (7780), 653-657 (2019).

60.   S. Zhang, in *Handbook of Materials Modeling : Methods: Theory and Modeling*, edited by W. Andreoni and S. Yip (Springer International Publishing, Cham, 2018), pp. 1-27.

61.   S. Zhang, T. Wei, J. Guan, Q. Zhu, W. Qin, W. Wang, J. Zhang, E. W. Plummer, X. Zhu, Z. Zhang and J. Guo, Physical Review Letters **122** (6), 066802 (2019).

62.   E. Suárez Morell, J. D. Correa, P. Vargas, M. Pacheco and Z. Barticevic, Physical Review B **82** (12), 121407 (2010).
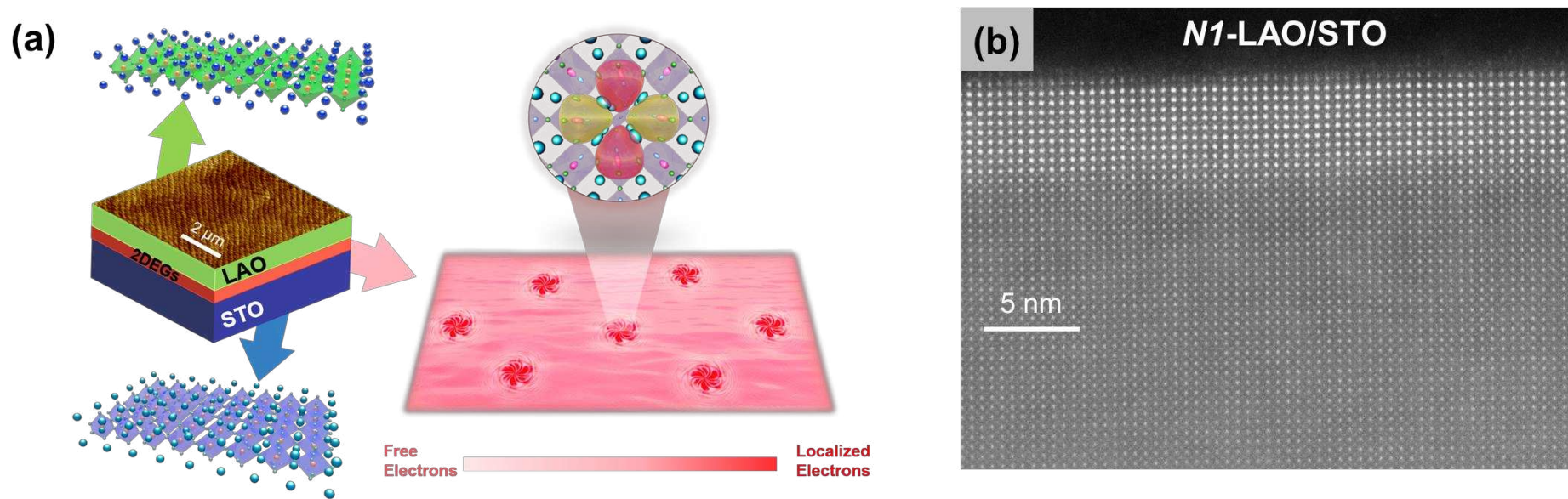
FIG 1. (a) Schematic displaying the formation of small polarons at the LAO/STO conducting interface with the AFM image for *N1*-LAO/STO indicating that the surfaces consist of clear atomic terraces. (b) Atomic resolution HAADF–STEM image of the representative *N1*-LAO/STO interface along the [001] zone axis. Note that the LAO thin-film is protected with Au thin-film before the preparation of TEM sample.
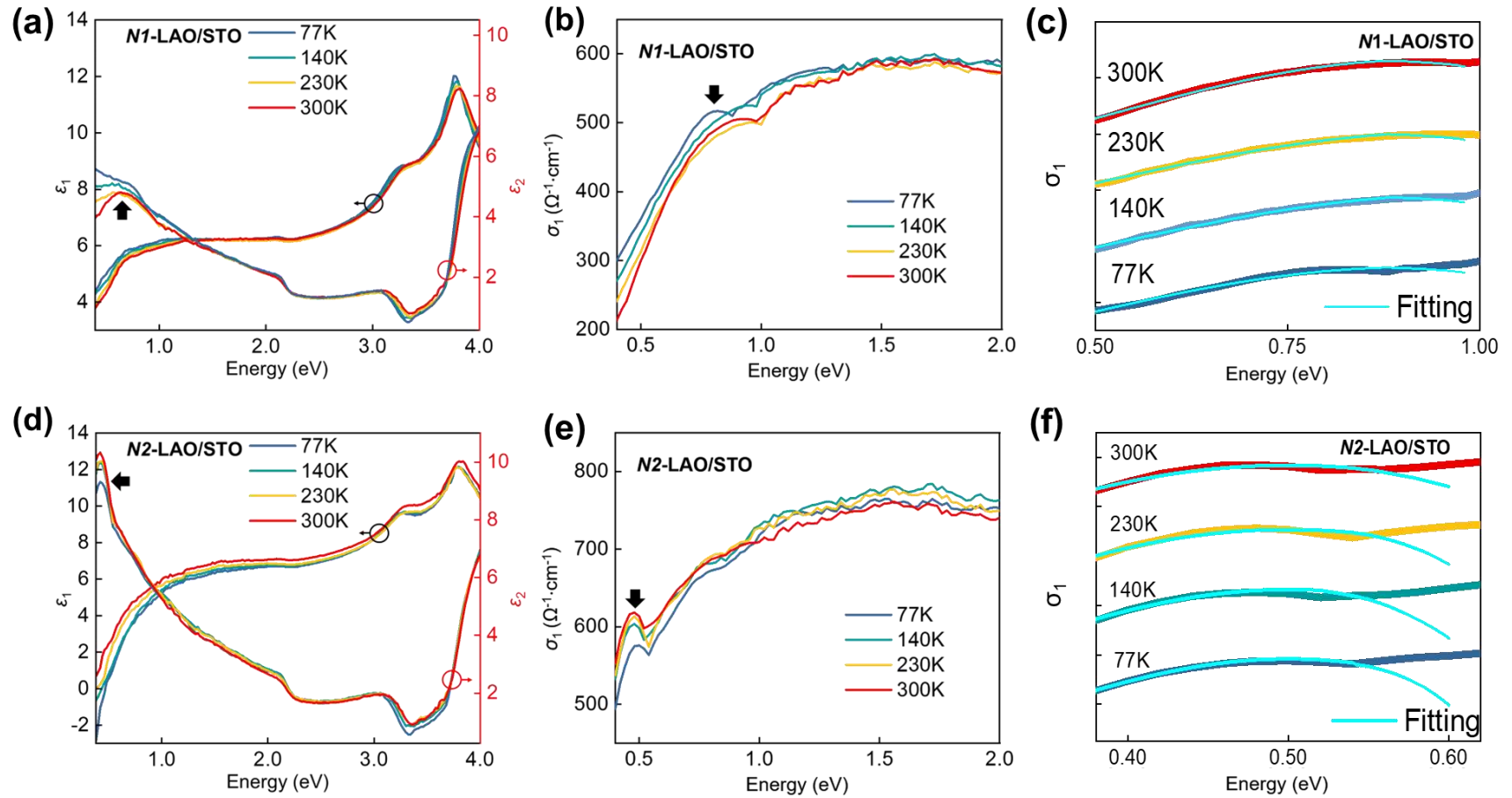
FIG 2. (a) Real, ε_1, and imaginary, ε_2, components of the dielectric function for *N1*-LAO/STO and their variations with temperature. (b) Temperature-dependent optical conductivity, σ_1, and (c) its stacked zoom-in spectra overlayed with the data fitting at the respective temperature using the Bryksin small polaron model for *N1*-LAO/STO. (d) Temperature-dependent real, ε_1, and imaginary, ε_2, components of the dielectric function for *N2*-LAO/STO. (e) Optical conductivity, σ_1, and (f) its stacked zoom-in spectra overlayed with the data fitting at the respective temperature using the Bryksin small polaron model for *N2*-LAO/STO.
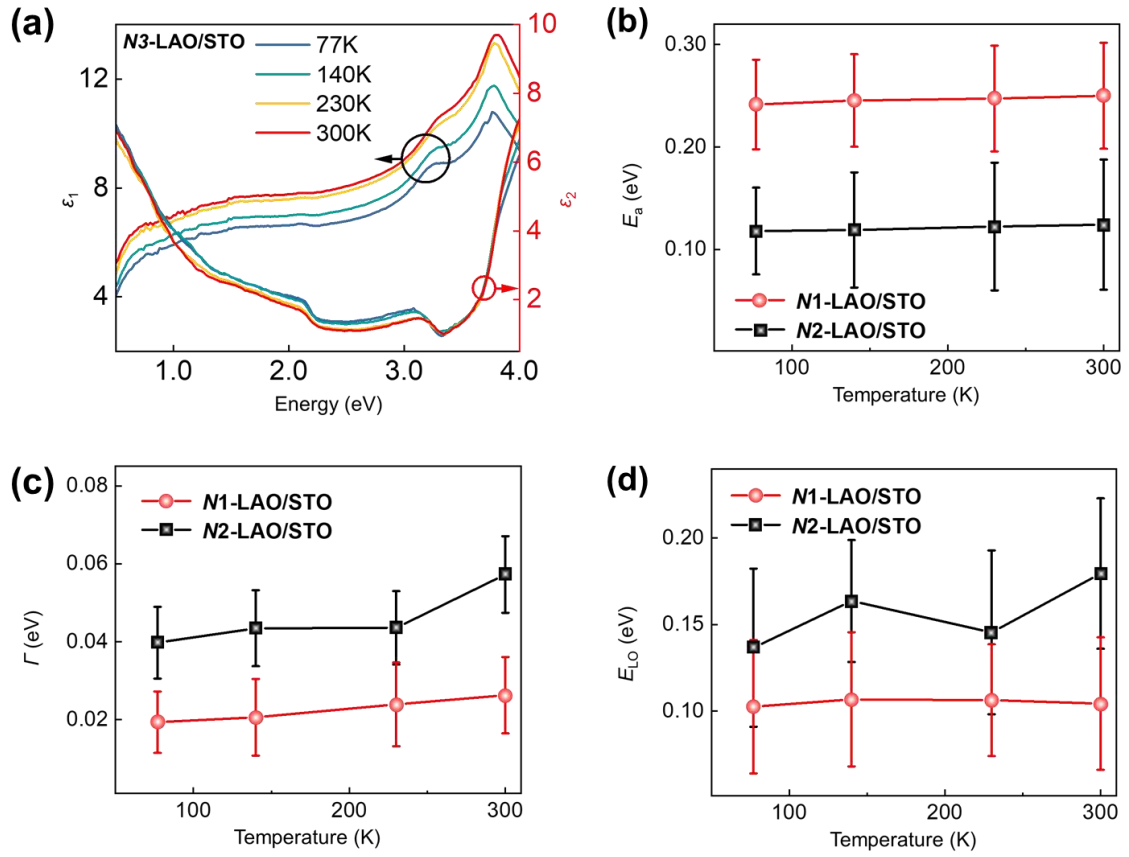
FIG 3. (a) Real, ε_1, and imaginary, ε_2, components of the dielectric function for the most conducting *N3*-LAO/STO interface. (b) Properties of the small polaron states of *N1*- and *N2*-LAO/STO derived using the Bryksin small-polaron model including the polaron activation or hopping energy, E_A. (c) The small polaron band width, Γ. (d) The phonon energy, E_{LO},
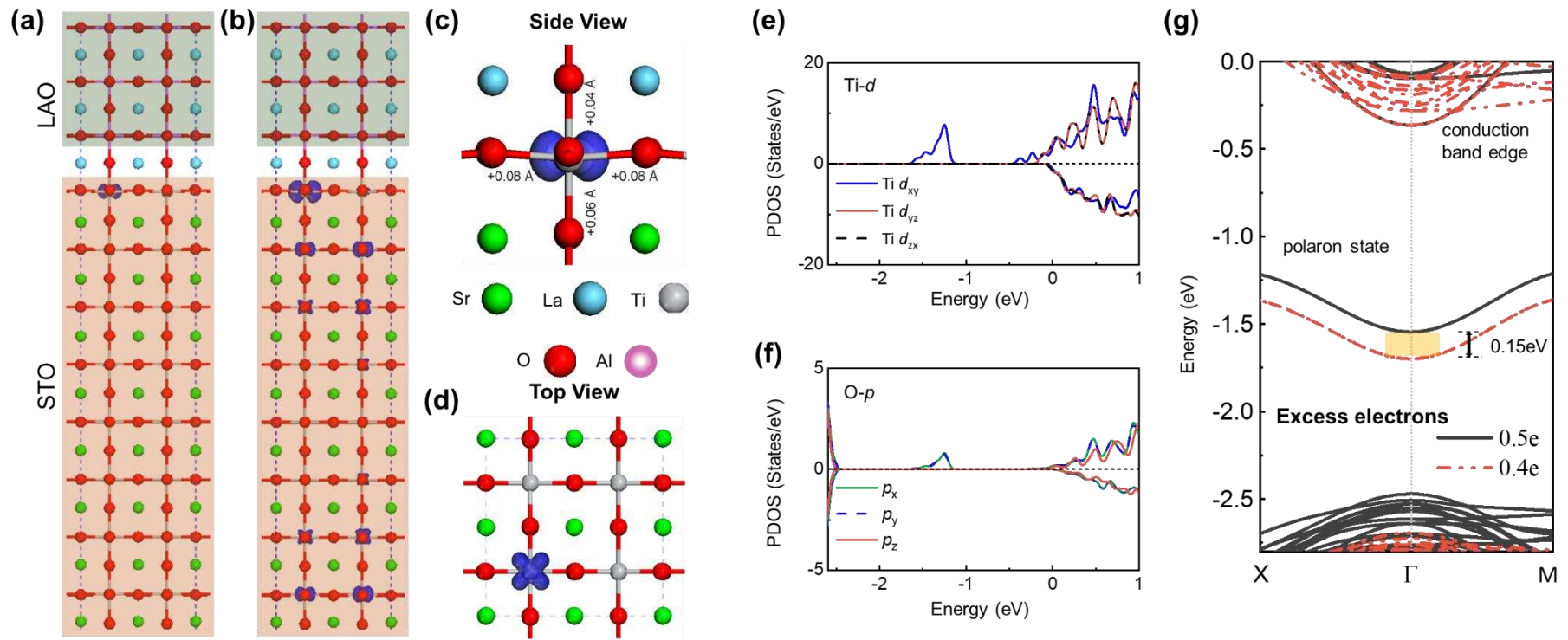
FIG 4. (a) The (LaAlO$_3$)$_{6.5}$/(SrTiO$_3$)$_{6.5}$ superlattice (side view) modelled for the DFT calculations. The partial charge density of the small polaron state is superimposed (blue shade) and visualized. (b) Penetration, and localization of charges at Ti lattice sites in the STO layer (blue superimposed surfaces) but localized charge concentration is sufficiently large for the small polaron formation only at the interface. (c) The side view of the LAO/STO interfacial structure. (d) The top view of the LAO/STO interfacial structure overlayed with the charge distribution of the small polaron states. The bond distortion is also denoted in the side view. (e) The Project density of states (PDOS) on the interfacial Ti-atom with the small polaron state. (f) The PDOS of the interfacial O-atom with the small polaron state. (g) The band structure (majority-spin) of (LaAlO$_3$)$_{6.5}$/(SrTiO$_3$)$_{6.5}$ superlattices with excess 0.5 electrons (black solid lines) and 0.4 electrons (red dashed lines) per unit cell. The relative shift of the small polaron states between the interfaces of different charge concentration is ~0.15 eV as highlighted by the yellow shade.

Supplementary Information

Detection of two-dimensional small polarons at oxide interfaces by optical spectroscopy

Chi Sin Tang,[1,2,3] Shengwei Zeng,[4] Jing Wu,[3] Shunfeng Chen,[1] Muhammad A. Naradipa,[4] Dongsheng Song,[5] M. V. Milošević[6], Ping Yang,[2] Caozheng Diao,[2] Jun Zhou,[3] Stephen J. Pennycook,[7,9] Mark B.H. Breese,[2,4] Chuanbing Cai,[1] Thirumalai Venkatesan,[10] Ariando Ariando,[4] Ming Yang,[8,*] Andrew T.S. Wee,[4,9,*] Xinmao Yin[1,*]

Affiliations:

[1]Shanghai Key Laboratory of High Temperature Superconductors, Department of Physics, Shanghai University, Shanghai 200444, China

[2]Singapore Synchrotron Light Source (SSLS), National University of Singapore, Singapore 117603

[3]Institute of Materials Research and Engineering, A∗STAR (Agency for Science, Technology and Research), 2 Fusionopolis Way, Singapore, 138634 Singapore

[4]Department of Physics, Faculty of Science, National University of Singapore, Singapore 117542

[5]Institute of Physical Science and Information Technology, Anhui University, Hefei 230601, China

[6]Departement Fysica, Universiteit Antwerpen, Groenenborgerlaan 171, B-2020 Antwerpen, Belgium

[7]Department of Materials Science and Engineering, National University of Singapore, Singapore, 117575, Singapore

[8]Department of Applied Physics, The Hong Kong Polytechnic University, Kowloon, Hong Kong, China

[9]Centre for Advanced 2D Materials and Graphene Research, National University of Singapore, Singapore 117546

[10]Center for Quantum Research and Technology, University of Oklahoma, Norman, Oklahoma 73019, USA

*Correspondence to: kevin.m.yang@polyu.edu.hk (M.Y.), phyweets@nus.edu.sg (A.T.S.W), yinxinmao@shu.edu.cn (X.Y.)

I. SAMPLE PREPARATION

A. Treatment of TiO$_2$-terminated STO Substrates to achieve atomic level smoothness.

Atomically-smooth TiO$_2$-terminated STO substrate is achieved via chemical treatment. Specifically, commercially available (001)-oriented STO substrates first undergo ultrasonic treatment in deionized water for 10 minutes. It is then dried by nitrogen gas. When the substrates are dried, they are then ultrasonically treated in buffered hydrofluoric acid (HF) solution for ~30 seconds to be dried once again by nitrogen gas. Finally, high-temperature annealing is conducted in a tube furnace at 950 °C for 1.5 hours in air with a temperature ramping up rate of 3 °C/min and ramping down rate of 5 °C/min.

Fig. S1 displays the AFM imaging of the STO substrate indicating its smoothness at the atomic level.

B. Crystalline LAO/STO Samples.

High-quality crystalline LaAlO$_3$/SrTiO$_3$ (LAO/STO) samples were prepared by growing LaAlO$_3$ film on top of the TiO$_2$-terminated (001) SrTiO$_3$ substrates using pulsed-laser deposition (PLD)[1, 2]. The crystalline LAO films were deposited using PLD (KrF laser λ=248 nm) at a temperature of 760°C. The laser repetition rate was 2 Hz with laser fluence set at 1.3 J/cm^2. The growth of crystalline LAO with a thickness of 8 uc (~3.56 nm) was *in-situ* monitored using reflection high-energy electron diffraction (RHEED) as seen in Fig. S7. Three samples labelled as *N1*-LAO/STO, *N2*-LAO/STO and *N3*-LAO/STO with increasing degree of oxygen vacancies. In order to control different degree of oxygen vacancies, different condition of deposition oxygen partial pressure and post annealing were performed. *N1*-LAO/STO was deposited at oxygen partial pressure P_{O2}= 1×10^{-4} Torr and then annealed at 550°C for 1 hour to remove the oxygen vacancies created during the deposition. *N2*-LAO/STO was deposited at P_{O2}=1×10^{-4} Torr and cooled down to room temperature at the same pressure. *N3*-LAO/STO was deposited at lower P_{O2}=1×10^{-6} Torr and then cooled down to room temperature at the same pressure. With the *N1*-LAO/STO annealed under high oxygen pressure, there should be little to no oxygen vacancies in this sample. For *N2*- and *N3*-LAO/STO which were deposited at low oxygen pressure without oxygen annealing, there will be oxygen vacancies in the samples and the oxygen vacancy density increases with decreasing P_{O2}. Fig. S2 shows the sheet resistance R_s, carrier density n_s, and Hall mobility μ_H as a function of temperature. All the sample show metallic behaviour all the way below 300 K. From N1 to N3-LAO/STO, the sample shows decreasing sheet resistance and increasing carrier density, indicate increase oxygen vacancy concentrate. The carrier concentrations of the samples are, *N1*-LAO/STO=9.4×10^{12} cm^{-2}, *N2*-LAO/STO=1.0×10^{14} cm^{-2}, and *N3*-LAO/STO=4.5×10^{16} cm^{-2} at 300 K.

To facilitate the eventual spectroscopic ellipsometry optical characterization (Section II.D), all three sets of LAO/STO samples have been roughened on their underside (i.e., single side polished) to minimize any form of back reflection (see discussion in Section II.D).

II. SAMPLE CHARACTERIZATION

A. HAADF-STEM Measurements. The cross-section HAADF-STEM samples were prepared using focused ion beam milling on a FEI Versa 3D machine. Thinning process is carried out with a low-energy Ar+ in the Bal-Tec Res-120 ion beam milling system. The HAADF–STEM imaging was collected at 200 kV using an ARM200CF microscope that is equipped with a cold field-emission electron gun and an ASCOR probe corrector. The collection angle for the HAADF–STEM imaging took place at 60–280 mrad with the convergence angle at 30 mrad.

B. High-resolution X-ray Diffraction (XRD) and Reciprocal Space Mapping (RSM) Measurements. To characterize the crystal structure of the $LaAlO_3$ (LAO) films on $SrTiO_3$ (STO) substrate, high-resolution X-ray diffraction experiments are performed at the X-ray Demonstration and Development (XDD) beamline at the Singapore Synchrotron Light Source (SSLS). Reciprocal space mappings (RSM) measurements are conducted by coplanar diffraction geometry. The lattice constants of LAO films are characterized based on the STO substrate. Figs. S3 –S5 display the RSMs around $(002)_{KL}$, $(002)_{HL}$, $(013)_{KL}$ and, $(-103)_{HL}$ for the *N1*-, *N2*- and *N3*-LAO/STO samples respectively. The concentrated film spots are clear indications that the LAO film is of premium quality.

C. XAS Characterization of Ti L-edge. To further confirm the differences in oxygen vacancy that brings about the differing carrier concentration between the 3 LAO/STO interfaces, X-ray Absorption Spectroscopy (XAS) is conducted with the Ti L-edge showing the core-level $Ti2p \rightarrow Ti3d$ transitions displayed in Fig. S6. At the current thickness of the LAO layer, the total electron yield signal is able to probe the 2D interface directly[3]. Results are consistent with the varying degree of charge density with respect to oxygen vacancy concentration. The spectra consist of four features attributed both to spin-orbit coupling ($2p_{3/2}$ and $2p_{1/2}$) and crystal-field (e_g and t_{2g}) splitting. With the progressive increase in interfacial oxygen vacancy from *N1*- to *N3*-LAO/STO, the intensity of the main peaks at ~457.6, ~460.0, ~463 and ~465.4 eV (yellow arrows) registers a decrease corresponding to a drop in Ti^{4+} concentration. Conversely, the progressive increase in intensity at ~458.5 and ~463.9 eV (black arrows) corresponds to the rise in Ti^{3+} concentration from *N1*- to *N3*-LAO/STO[3, 4]. These collective trends of the drop in Ti oxidation states provide clear evidence of the increase in oxygen vacancy concentration from *N1*- to *N3*-LAO/STO that leads to the increase in interfacial delocalized charge concentration as confirmed by our transport measurements displayed in Fig. S2.

D. Spectroscopic Ellipsometry Measurements. Optical characterization measurements are conducted using the J. A. Woollam Co., Inc spectroscopic ellipsometer with the photon energy of 0.38–4.55 eV with a photon energy step size of (0.0200±0.0004) eV. Ellipsometric parameters, Ψ (ratio of the amplitude between *p*-and *s*-polarized reflected light), and Δ (phase difference of the *p*-and

s-polarized reflected light) are obtained from the optical measurements conducted under high-vacuum conditions with a base pressure of 1×10^{-9} mbar at temperatures between 77 and 300K in a high-vacuum chamber. At each photon energy point, measurement requires ~30 consecutive measurements of the Ψ and Δ parameters where each parameter must fall within the error of ±0.05 before obtaining an average value. Any measured parameter that falls out of this error margin will be discarded. The STO substrate has also been measured at similar temperature points under the same high-vacuum conditions and the fitting of the raw Ψ and Δ parameters takes into consideration roughness of the substrate surface. The dielectric coefficients, $\varepsilon(\omega)=\varepsilon_1(\omega)+i\varepsilon_2(\omega)$, of the LAO/STO interface are extracted from the parameters Ψ and Δ via an air/LAO/Interface/STO multilayer model, where the interface layer consist of a uniform composite heterointerface component. All three sets of LAO/STO samples have been roughened on their backside to minimize any forms of back surface reflection which may complicate the fitting process. Meanwhile, the beam spot of incident light source is kept at the centre of the sample and is sufficiently small (~3×3 mm) to prevent any spurious reflections and light scattering from the sample edges. These further reduce the effects of light scattering and spurious signals which may affect the measurement results. At each photon energy point, measurement requires 30 consecutive measurements of the Ψ and Δ parameters where each parameter must fall within the error of ±0.05 before obtaining an average value. All 30 measured data at each energy point are within this error range and any measured parameter that falls out of this error margin will be discarded. The optical data of the interfacial film layer is derived by eliminating the optical signals from the top LAO and bottom STO layers. Hence, the final optical signal from the interfacial layer is not just an overlap of optical signals of the top LAO film and STO substrate but registers the optical signal because of the interfacial influence from both LAO and STO surfaces. As SE has no charging issue due to its photon-in-photon-out methodology, we can study simultaneously the complex dielectric response of the LAO/STO[5].

In addition, SE measurements differ from optical other techniques such as photoluminescence measurement in that the SE detector only registers the sample optical responses at the respective photon energy. Hence, the effects of higher harmonic that leads to higher energy optical features can be omitted.

The parameters Ψ and Δ, are expressed as follows

$$\tan \Psi \exp(i\Delta) \equiv \frac{r_p}{r_s} \qquad (1)$$

where $r_{p(s)}$ is the reflectivity of the *p*-(*s*-) polarized light. Since $\tan \Psi$ and Δ are ratios of the intensity and phase, respectively, of the *p*- and *s*-polarized light, it ensures that these quantities are self-normalized

Based on the Fresnel equations, the quantities are expressed as

$$r_p^{ij} = \frac{n_j \cos \theta_i - n_i \cos \theta_j}{n_j \cos \theta_i + n_i \cos \theta_j} \qquad (2)$$

and

$$r_s^{ij} = \frac{n_j \cos \theta_i - n_i \cos \theta_j}{n_j \cos \theta_i + n_i \cos \theta_j} \qquad (3)$$

In the above equations, n and θ represent the index of refractive and incident angle, respectively. The subscripts i and j represent the two materials. The complex dielectric function $\varepsilon(\omega) = \varepsilon_1(\omega) + i\varepsilon_2(\omega)$ of media are derived using

$$\sqrt{\varepsilon(\omega)} = n(\omega) \qquad (4)$$

where ω denotes the photon frequency.

In multi-layered systems, phases differences of the waves and interference effects must be accounted for. In typical 2-layer thin-film on substrate systems (vacuum/film/substrate), the reflectivity can be expressed in the following

$$r_{vac,multi} = \frac{r_{vac,film} + r_{film,sub} \, \exp(i2\delta_{film})}{1 + r_{vac,film} \cdot r_{film,sub} \, \exp(i2\delta_{film})} \qquad (5)$$

Where

$$\delta_{film} = \frac{2\pi d_{film}}{\lambda} n_{film} \cos \theta \qquad (6)$$

Subscripts *vac* and *multi* denote the vacuum and film-substrate layer, respectively. δ_{film} is the phase change of the incident wave of wavelength, λ, as it penetrates the film layer with thickness d_{film}.

In the case of the LAO/STO system, it comprises three layers: the top LAO film, a conducting 2DEG interface layer in between, and the bulk STO substrate below. Each section is assumed to have uniform distribution.

Using the analysis of wave propagation in a stratified medium, reflectivity of three-layered system is expressed using Fresnel equation

$r_{vac,multi}$

$$= \frac{r_{vac,LAO} + r_{LAO,int} \exp(i2\delta_{LAO}) + r_{vac,LAO} \cdot r_{LAO,int} \cdot r_{int,STO} \exp(i2\delta_{int}) + r_{int,STO} \exp(i2(\delta_{LAO} + \delta_{int}))}{1 + r_{vac,LAO} \cdot r_{LAO,int} \exp(i2\delta_{LAO}) + r_{LAO,int} \cdot r_{int,STO} \exp(i2\delta_{int}) + r_{vac,LAO} \cdot r_{int,STO} \exp(i2(\delta_{LAO} + \delta_{int}))}$$

$$(7)$$

where

$$\delta_i = \frac{2\pi d_i}{\lambda} n_i \cos \theta_i \qquad (8)$$

Where d represents the layer thickness (LAO film and interface). Subscripts *vac*, *multi*, and *int* denotes the vacuum, LAO/STO multilayer, and the interfacial layer, respectively. Alongside the LAO and STO materials, these are materials involved in the photon propagation. In equation (S5), the dielectric function, $\varepsilon(\omega)$, of bulk STO substrate can be measured independently while the thickness, d_{LAO}, of the LAO film is estimated to be ~3.56 nm (8 u.c.).

Interfacial thickness of the LAO/STO layer is first determined via an angle-dependent ex-situ measurement at angles 60°, 65° and 70° from the sample normal. This provides 3 sets of Ψ and Δ data, with 3 equations for a self-consistent iterative process. Iteration of the SE data can be performed based on equations S2 and S9. With the thickness of the 2DEG falling in the range ~2—7nm[6-12], the initial guess for d_{int} is set at 5nm. Likewise, initial $\varepsilon(\omega)$ for the LAO film is set as that of bulk LAO (Figs. S8(b) and (d)) that can be separately measured where the substrate surface roughness is taken into consideration during the fitting process.

With d_{int} and $\varepsilon(\omega)$ for the LAO layer fixed, equation S1 is fitted using the experimental values of Ψ and Δ measured at $\theta=60°$ by adjusting the $\varepsilon(\omega)$ of interface layer. Thereafter, the newly fitted $\varepsilon(\omega)$ belonging to the interface is fixed, during which, d_{int} is adjusted to ensure that equation S1 can be fitted into the experimental parameters Ψ and Δ measured *ex-situ* at $\theta=65°$. Following which, the adjusted d_{int} is fixed with the previously fitted interfacial $\varepsilon(\omega)$, and the experimental parameters of Ψ and Δ measured at $\theta=70°$ is fitted using equation S1 to adjust the $\varepsilon(\omega)$ of LAO film layer.

This iterative process is repeated by returning to the Ψ and Δ parameters measured at $\theta=60°$ and the other incident angles, with only 1 variable while keeping the other 2 kept constant. This iterative process stops only when all 3 parameters – d_{int}, $\varepsilon(\omega)$ of LAO and the interfacial layer – are consistent with equation S1 for all incident angles 60°, 65° and 70°. Note that the iterative results obtained for d_{int} stands at ~5.2 nm for all three samples *N1*-, *N2*- and *N3*-LAO/STO. Based on this analytical methodology, the surface roughness subsumes under the interfacial layer during the data fitting process and d_{int} should not fall below the thickness of 1 uc so that interfacial roughness could be accounted for[5]. With a fitted interfacial thickness of ~5.2 nm, our analysis has sufficiently accounted for any forms of roughness that arise from either the STO substrate or the interface itself.

Along with the known optical properties of the STO substrate (Fig. S8(a) and (c)), the LAO thickness, these parameters can then be used in determining the temperature-dependent optical properties of the LAO film layer of all three samples which are measured at 70° during the *in-situ* SE measurements with the raw Ψ and Δ parameters elucidated as seen in Figs. S9—S11. To eventually elucidate the optical parameters in the form of the dielectric function $\varepsilon(\omega) = \varepsilon_1(\omega) + i\varepsilon_2(\omega)$, from the raw Ψ and Δ parameters, point-by-point fitting is conducted in this study where it consists of fitting the experimental data one photon energy at a time instead of the entire spectrum at one go. The data at

each photon energy point is fitted by varying all the defined fitting parameters in order to obtain the eventual optical data as presented in our study. Both the real ε_1 and imaginary ε_2 spectra of *N1*, *N2* and *N3*-LAO/STO (main text Figs. 2 and 3) show Kramers-Kronig consistency and are in good agreement with previous studies[13].

III. SMALL POLARON ANALYSIS

A. Bryksin Small-polaron Theoretical Model. The Bryksin small-polaron theoretical model which accounts for small-polaron optical absorption is employed to model our temperature-dependent optical spectra[14-16]. The expression is used in the analysis of systems with strong electron-phonon coupling and that it accounts for polaron hopping in the energy region close to the fermi level.

This theoretical model allows for the analysis of the polaron response in the σ_1 spectra and it can be defined in 3 regimes.

Namely, in the energy region below the polaron peak (by definition, $\hbar\omega < 4E_a[1 - (\mu E_{LO}/\Gamma^2)]$),

$$\sigma_1(\omega) \approx A \exp\left(-\frac{\mu^2}{\Gamma^2}\right) \exp\left(-\frac{(\hbar\omega - 4E_a)^2}{8E_a E_{LO}}\right) \qquad (9a)$$

Where μ: Fermi energy; E_a: small polaron hopping energy, Γ: Polaron band width, and E_{LO}: phonon energy

In the photon energy region around the polaron peak (by definition, in the range $4E_a[1 - (\mu E_{LO}/\Gamma^2)] < \hbar\omega < 4E_a[1 + (\mu E_{LO}/\Gamma^2)] + 2\mu$),

$$\sigma_1(\omega) \approx A \exp\left(-\frac{\mu^2}{2\Gamma^2}\right) \exp\left(-\frac{(\hbar\omega - 4E_a - \mu)^2}{8E_a E_{LO} + 2\Gamma^2}\right) \qquad (9b)$$

And at the high photon energy region above the polaron peak (by definition, $\hbar\omega > 4E_a[1 + (\mu E_{LO}/\Gamma^2)] + 2\mu$)

$$\sigma_1(\omega) \approx A \exp\left(-\frac{(\hbar\omega - 4E_a)^2}{8E_a E_{LO} + 4\Gamma^2}\right) \qquad (9c)$$

Since the polaron peak is observed in the σ_1 spectra, the expression of the Bryksin small polaron model in the intermediate range (i.e., Supplementary equation 9b) is employed for the curve fitting analysis.

If one can further assumed that the Fermi level is located at μ=0. Supplementary equation 9b can be further simplified as[14, 15]:

$$\sigma_1(\omega) \approx A \exp\left(-\frac{(\omega - 4E_a)^2}{8E_a E_{LO} + 2\Gamma^2}\right) \qquad (10)$$

Where the main fitting parameters includes E_a: small polaron hopping energy, Γ: Polaron band width, and E_{LO}: phonon energy. In which case, the maximum of the polaronic line-shape lies at $\hbar\omega_0 \approx 4E_a$.

Nevertheless, for the purpose of analysing the small polaron feature at the LAO/STO interface, Supplementary equation 9(b) is employed where the Fermi level, μ, is set at ~1.38 eV for $N1$-LAO/STO and ~1.25 eV for $N2$-LAO/STO. These values are first based on the location of the small polaron state at ~1.14 eV below the fermi level based on PDOS calculations (main text Figs. 4(e) and (f)) and that the polaron activation energy derived from the optical data (main text Figs. 2(b) and (e)) is estimated to be ~0.24 eV for $N1$-LAO/STO and ~0.11 eV for $N2$-LAO/STO.

From the experimentally derived $\varepsilon_2(\omega)$ spectra, comparison with the theoretical optical conductivity model, $\sigma_1(\omega)$, based on the following

$$\sigma_1(\omega) = \omega\varepsilon_0\varepsilon_2(\omega) \qquad (11)$$

Where ε_0 denotes the permittivity of free space.

Using Supplementary equation 10, curve fitting is then conducted for the respective σ_1 spectra in the photon energy region where the polaron peak is located. With the reduced chi-square statistics conducted during the curve fitting process, the error bars for the respective fitting parameters, E_a, E_{LO}, and Γ are derived.

The compatibility between the optical features in the respective σ_1 spectra and the Bryksin small-polaron model alongside the considerably reasonable fitting error (as denoted by the error bars) are indications that these optical responses are indeed signatures of small polaron present at the LAO/STO interface.

B. Temperature-Dependent Polaron Analysis. Temperature-dependent parameters derived from the fitting analysis of the σ_1 spectra provide crucial information pertaining to the temperature effects on the polaronic feature and the charge-lattice interaction that contributes to the formation of the polaron at the LAO/STO 2D-interface. Fig. 3(a) displays the temperature-dependent evolution of the polaronic activation energy, E_a, band width, Γ, and phonon energy, E_{LO}, of $N1$-LAO/STO. Fig. 2(b) displays the temperature-dependent optical conductivity spectra, σ_1, of $N1$-LAO/STO derived from the ε_2 spectra using Supplementary equation 11. The Drude response observed in the ε_2 spectra is significantly redshifted below the instrument energy range due to the feature of Supplementary Equation 11. Nevertheless, the mid-gap previously identified as the interfacial 2D polaron peak remains prominent within the spectral range between ~0.82 and ~0.98 eV and that the aforementioned asymmetric optical structure that is characteristic of small polaron remains[17].

The Bryksin model which accounts for small-polaron optical absorption is employed to analyze the optical spectra[18]. It is used for systems with strong electron-phonon coupling where small-polaron hopping in the energy region close to the Fermi level takes place. Based on the expressions of the Bryksin model (Supplementary Equations 9 and 10), the temperature-dependent parameters which

include the hopping energy, E_a, bandwidth, Γ, and phonon energy, E_{LO}, of the 2D interfacial polarons can be derived.

Figs. 2(c) and 2(f) display a very good fit between the experimentally measured polaron response and the theoretical Bryksin small-polaron model for both *N1*- and *N2*-LAO/STO interfaces, respectively, throughout the entire temperature range. The compatibility clearly indicates that the near-infrared responses in both *N1*- and *N2*-LAO/STO interfaces are of small-polaron origin. This observation of LAO/STO interfacial small polarons is notably distinct from the previous study where the interfacial charges have been identified as large polarons[19].

Hopping energy, E_a. Fitting analysis yielded very marginal increase of E_a from ~0.244 eV to ~0.249 eV between 77 and 300K. Despite the polaronic wave functions being more energetic leading to a greater wavefunction spread with rising temperature, this effect is outweighed by the increase in incoherent scattering on the thermally populated phonon modes. Besides, contribution to an increase in E_A is further expected in a disordered system with rising temperature because the difference in energy between initial and final states is increased[20, 21]. These two contributing factors eventually lead to a marginal increase in E_a with temperature. The distinct reduction in E_a of *N2*-LAO/STO compared to *N1*-LAO/STO may be partially attributed to the increase in overlapping potential wells due to higher oxygen vacancies at the interface that allows for a greater ease of interstitial charge hopping. Comparison of E_a between *N1*-LAO/STO and *N2*-LAO/STO further suggests that an increase in interfacial charge density has a greater influence on the interfacial polarons than temperature.

Polaron band width, Γ. There is also a very gradual monotonic broadening in the polaron band width, Γ, from ~0.011 to ~0.033eV with temperature. This can be attributed to the increased in energy of both the lattice charge carriers which allows for a growing number of polaron transition to the conduction band states alongside an increase in incoherent scattering attributed to thermally populated phonon modes[19]. This eventually leads to an extended distribution of polaron energies as manifested through the peak broadening effect. This temperature trend corresponds with small-polarons behaviour where phonon broadening of the local electronic energy levels progressively broadens the absorption bands[17]. The larger bandwidth of *N2*-LAO/STO may be attributed to the increase in conduction band states formed by oxygen vacancy sites occupied by polarons. Thereby, leading to an extended distribution of polaron energies as manifested through a wider peak width[14, 15].

Phonon energy, E_{LO}. The phonon energy shows no clear temperature-dependent behaviour with fluctuation between ~0.11 and ~0.14eV. This phonon energy range lies relatively close to the hard longitudinal optical (LO) phonon mode, LO3, belonging to the STO substrate[22]. As the only available phonon mode in this energy range and that it has the highest coupling constant compared to other LO-modes[23], we can attribute the formation of this small-polaron to the electron-phonon interaction via

the LO3 mode calculated to be ~0.1 eV[19]. This fluctuation in phonon energy can be attributed to the presence of interfacial lattice strain and other interfacial factors such as electric field, phonon coupling across the interface and the propagation of the LAO lattice distortion into the STO layer[24]. Considering the role that LO3 plays in the interfacial polaron formation, the larger E_{LO} magnitude for $N2$-LAO/STO may be attributed to structural changes due to electrostatic doping by the increase in oxygen vacancies[25] or possible weaker coupling to additional phonon modes. Generally, phonon mode analysis highlights the critical role that electron-phonon interaction plays in the formation of this 2D interfacial polaron.

Small Polaron Analysis at different interfacial charge concentration. Having ascertained the polaronic origin of the near-infrared optical response at the $N1$-LAO/STO interface, we further investigate how an increase in interfacial carrier concentration affects the electron-phonon coupling dynamics and modifies the polaronic response.

Fig. 2(d) displays the temperature-dependent ε_1 and ε_2 spectra, respectively, of $N2$-LAO/STO. Similar to $N1$-LAO/STO interface, both spectra possess similar optical features with those reported in previous studies. There is also an increase in the Drude response intensity attributed to higher interfacial carrier concentration. Notably, the mid-gap previously attributed to the polaron response persists at the $N2$-LAO/STO interface across all temperature. Nevertheless, the polaron peak is redshifted to ~0.42 eV alongside a slight broadening. Similarly, the Bryksin model is used to analyze the temperature-dependent behaviour of the polaron responses of $N2$-LAO/STO when converted to the σ_1. While the Drude response is red-shifted below the spectral range, the polaron peak remains prominent [Fig. 2(e)]. Polaron peak fitting of the σ_1 spectra also yielded very favourable results [Fig. 2(f)] with the polaron activation energy, E_a, redshifted significantly lower (Fig. 3 and Section III.B)

Introduction of more oxygen vacancies to the LAO/STO interface leads to further increase in carrier density (~1×10^{16} cm^{-2}) and further modifies the ε_1 and ε_2 spectra of $N3$-LAO/STO [Fig. 3(a)]. Although the general optical features of $N3$-LAO/STO remains, there is a growing temperature-dependence particularly with a marked intensity increase of the ε_1 spectra. Meanwhile, the ε_2 spectra also undergo a significant change in the low-energy region where the near-infrared polaron peak previously observed in both $N1$- and $N2$-LAO/STO is further redshifted to photon energy below the instrument spectral limit. Hence, temperature-dependent analysis of the small polaron response will be restricted to the $N1$- and $N2$-LAO/STO interfaces.

Figs. 3(b) to 3(d) compare the hopping energy, E_a, band width, Γ, and phonon energy, E_{LO}, respectively, of the 2D interfacial polarons at the $N1$- and $N2$-LAO/STO interfaces. E_a of $N2$-LAO/STO falls significantly lower to ~0.12 eV compared to $N1$-LAO/STO's ~0.23 eV. Between 77 and 300 K, temperature-dependence of E_a of both $N1$- and $N2$-LAO/STO follows similar trend with a slight but apparent increase with rising temperature as it becomes easier for the electron to move

from one Ti-site to the next[17]. The distinct reduction in E_a of 2-LAO/STO compared to N1-LAO/STO may be partially attributed to the increase in overlapping potential wells due to higher oxygen vacancies at the interface that allows for a greater ease of interstitial charge hopping. Comparison of E_a between N1-LAO/STO and N2-LAO/STO further suggests that an increase in interfacial charge density has a greater influence on the interfacial polarons than temperature.

The polaron bandwidth, Γ, of N2-LAO/STO is slightly larger than N1-LAO/STO (main text Fig. 3c). Nevertheless, both display similar temperature-dependent trends with a monotonic width broadening from ~0.03 to ~0.07 eV for N2-LAO/STO and relatively smaller increase of ~0.01 to ~0.28 eV for N1-LAO/STO. This progressive broadening with rising temperature is consistent with the behaviour of small-polarons which corresponds with the phonon broadening of the local electronic energy levels which in turn progressively broadens these absorption bands[17]. The relatively larger bandwidth belonging to N2-LAO/STO compared to N1-LAO/STO may be attributed to the increase in conduction band states formed by oxygen vacancy sites occupied by polarons. Thereby, leading to an extended distribution of polaron energies as manifested through a wider peak width[14, 15].

Finally, the E_{LO} of both N1- and N2-LAO/STO does not display any clear temperature trend [Fig. 3(b)]. Instead, the value fluctuates between ~0.14 –0.18 eV for N2-LAO/STO and ~0.11—0.13 eV for N1-LAO/STO. These values are marginally larger but remains consistent with the hard longitudinal optical phonon, LO3, associated to the LAO/STO interfacial polaron[19, 23, 26]. The presence of LO3 phonon mode plays an important role in controlling the 2D interfacial carrier mobility[19]. Considering the role that LO3 plays in the interfacial polaron formation, the larger E_{LO} magnitude for N2-LAO/STO may be attributed to structural changes due to electrostatic doping by the increase in oxygen vacancies[25] or possible weaker coupling to additional phonon modes. Generally, phonon mode analysis highlights the critical role that electron-phonon interaction plays in the formation of this 2D interfacial polaron.

Based on the experimental analysis of both N1- and N2-LAO/STO, the prominent temperature-dependent and the asymmetric peak features are clear indications of small polaron present at the LAO/STO interfaces. Moreover, these temperature-dependent behaviours allow us to rule out the contribution of large polaron to these optical features whose features are independent of temperature[17].

IV. ELIMINATING OTHER POSSIBLE CONTRIBUTING FACTORS TO THE OPTICAL RESPONSES

Besides ruling out the possibility of defect states contributing to the formation of the near-infrared optical response, we rule out any other possible factors that may lead to the optical features in main text Fig. 2. The presence of exciton may be omitted because while exciton weakens significantly with rising temperature[27, 28], the near-IR feature detected at the LAO/STO interface has a trend contrary to that of exciton with an intensity increase with temperature.

With the vanishingly small ferromagnetic response contributed by the LAO/STO interface[29], the onset of magnons can also be omitted. Finally, any contribution by plasmon excitation can also be ruled out due to detection of plasmon requires the simultaneous presence of a zero-crossing in the ε_1 spectrum alongside a prominent peak feature in the Loss-function spectrum which are not present in the respective components of the dielectric functions[30, 31].

Therefore, by eliminating these possible contributing factors, the polaronic origin of these mid-IR peaks at the LAO/STO interface can be safely concluded.

V. FIRST-PRINCIPLES CALCULATIONS

A. Model Setup. All first-principles calculations were conducted using Vienna Ab-initio Simulation Package (VASP.5.4.4.18)[32, 33], with the projector-augmented-wave (PAW) method[34] for the electron-ion interaction and the Perdew–Burke–Ernzerhof (PBE) parameterized exchange–correlation functional. The cut-off energy for the electronic plane-wave expansion was set to 500 eV for all calculations. The total energy converged below 10^{-5} eV and the force on each atom was relaxed to be smaller than 0.01 eV/Å. The on-site Coulombic interactions were treated by using the PBE+U method with an effective Hubbard $U = 4.0$ eV for Ti d orbitals and 8.0 eV for La f orbitals[35]. The first-Brillouin zones of $SrTiO_3$ (STO) and $LaAlO_3$ (LAO) bulks, and the unit cell and (2×2×1) supercell of LAO/STO (001) heterostructure were sampled by Monkhorst-Pack based 8×8×8, 8×8×1 and 4×4×1 k-point meshes, respectively. Based on these settings, the calculated lattice constants of LAO and STO bulks are 3.78 Å and 3. 97 Å, respectively, in good agreement with experimentally derived values[36].

The $LaAlO_3/SrTiO_3$ (001) interface was modelled by using a $(LaAlO_3)_{6.5}/(SrTiO_3)_{8.5}$ superlattice, as illustrated in main text Fig. 4(a). With its effectiveness in simulating the insulator-metal transition at LAO/STO interface, the LAO/STO superlattice method is widely utilized in the computational study of the interfacial charge transfer processes of the LAO/STO system[37-40]. The in-plane lattices were fixed to the optimized lattice constant of the STO bulk, while the out-of-plane lattice constant and all the atomic positions in the superlattice were relaxed. This superlattice structure can model excess 0.5 electrons (~3.2×10^{14} cm^{-2}· u.c.$^{-1}$) at the interface, leading to two identical n-type conducting interfaces (TiO_2/LaO)[38]. The quantity of charge transfer from the LAO to the STO substrate layer converges to half an electron per two-dimensional unit cell (i.e., 0.5e^-/uc) with increasing layer number above the threshold 4 uc. The charge transfer quantity of 0.5e^-/uc can be calculated by the integration of the corresponding partial charge of the transferred electron on the side of the STO substrate (the density of states from the fermi level and down to -2 eV).

Further confirmation of the 0.5e^-/uc electron-transfer is made using different exchange-correlational functionals (LDA and GGA-PBE) and U values (where U=4.0 and 2.0 for Ti3d), as displayed in Fig. 12. In this case, with different exchange-correlational functionals considered, an electron transfer of

0.5 e^-/uc to the interface is still achieved, and PBE functional with U=4.0 can produce the decayed charge density from the interface into STO bulk. Thus, by using PBE functional and Hubbard U=4.0, the 0.5 e transfer is still yielded. Furthermore, it is important to note that the U parameters used in this study is comparable with a previous study[41] and the results yielded are consistent with the experimental result.

The polaron state was simulated by breaking the symmetry of the two TiO_2 interfacial layers, in which, the Ti-O bonds in an octahedral TiO_6 were stretched in the (2×2×1) LAO/STO (001) supercell before the structural optimization. For the non-polaron state, the superlattice structure was optimized without this initial perturbation. This method has been widely used to study the polaronic effect in transition metal oxides[42-45]. We also considered less conducting interface by reducing the number of total valence electrons of the superlattice. As Fig. S14(a) shows, the reduced electrons are from the excess electrons in the Ti atoms, which results in 0.4 electrons at the interface ($\sim 2.56 \times 10^{14}$ cm^{-2}· u.c.$^{-1}$).

B. Polaron Formation Energy. The polaron formation energy, E_{Pol}, quantifies the stability of a small polaron that is dependent on the interplay between the structural changes to induce the lattice deformation to accommodate the electrons, E_{Def}, and the electronic energy gained by localizing the electrons, E_{Loc}. The formation energy can be expressed according to the equation[46, 47]:

$$E_{Pol} = (E_{Def} - E_{Loc})/N_p \qquad (12)$$

Where N_p denotes the number of small polarons.

The formation energy can also be derived by the following expression

$$E_{Pol} = (E_p - E_{np})/N_p \qquad (13)$$

Where E_p and E_{np} denote the energy of both the polaron and non-polaron states, respectively.

As displayed in Fig. S14, the polaron state is more energetically stable in LAO/STO interfaces with higher electron density. This indicates the stability of the small polarons depends on the density of excess electron due to effects of electronic correlations. With a greater density of excess electrons, the corresponding increase in repulsion between the electrons enhances the attraction as quantified by E_{Loc}, the electronic energy gained by localizing the electrons due to the interaction between the small polaron associated electron and the Ti lattice site. This in turn stabilizes the small polaron upon its formation.

VI. SUPERCONDUCTIVITY AT OXIDE INTERFACE WITH POLARONIC STATE & ANALOGOUS RELATIONSHIP WITH MAGIC-ANGLE TWISTED BILAYER GRAPHENE

This study holds important implications in unravelling the role that quasiparticle dynamics play in governing superconductivity at the perovskite oxides heterointerfaces and is potentially analogous to other heterostructure systems and especially that of the twisted bilayer graphene system[48, 49]. In the strong interactions between the excess interfacial electrons and the Ti lattices to form the polaronic states, the distortion of the LAO/STO lattice invariably breaks the periodic lattice symmetry[50, 51]. Meanwhile, our calculations show that the formation of small polarons due to the considerable loss in electron kinetic energy results in the significant reduction in bandwidth of these polaron states to ~0.5 eV as compared to ~1.2 eV in the free electron states. This band flattening process facilitates the electron-electron correlations and holds the key to the emergence of superconductivity at the LAO/STO interface[52-55]. This superconductive mechanism in perovskite oxide interfaces bears strong resemblance to the unexpected superconductivity in the magic-angle twisted bilayer graphene with an interlayer misalignment of 1.1°[48, 56]. In which case, their underlying mechanism are analogous with the emergence of flat electronic bands at certain twist angles in the moiré superlattice as a result of interlayer misalignment[48, 56]. Specifically, the formation of the Moiré patterns breaks the original periodic structure, not only does the inhomogeneity of the electron systems lead to a drastic reduction of the Fermi velocity, a significant modification to the electronic properties, leading to the formation of flat bands at the Fermi level which facilitates the onset of the superconductive states[57-59]. Similar to the 2D superconductivity at perovskite oxide interfaces, the emergence of strong electron-electron interactions because of broken periodic lattice symmetry holds the key to the onset of superconductivity in magic angle twisted bilayer graphene[60].
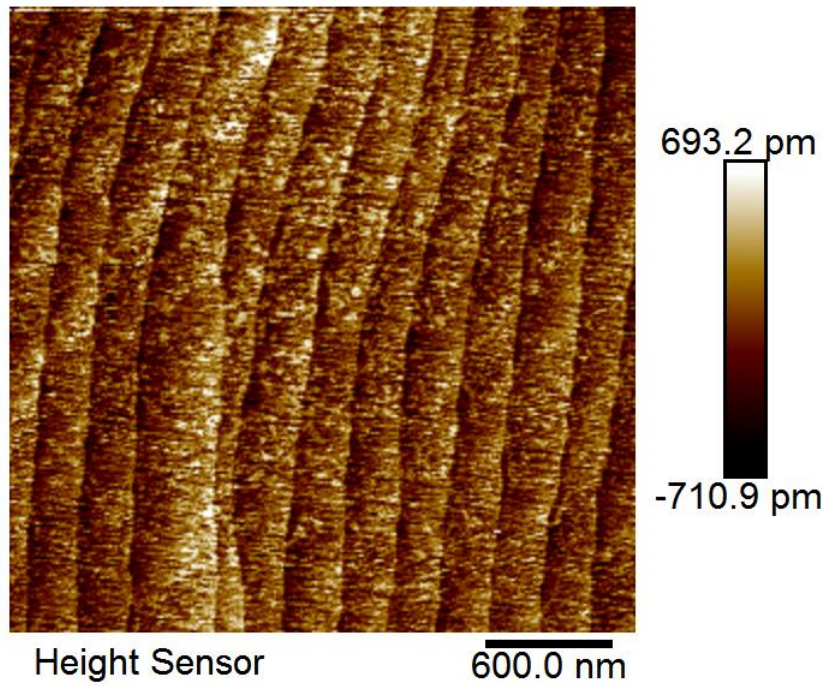
VII. SUPPLEMENTARY FIGURES

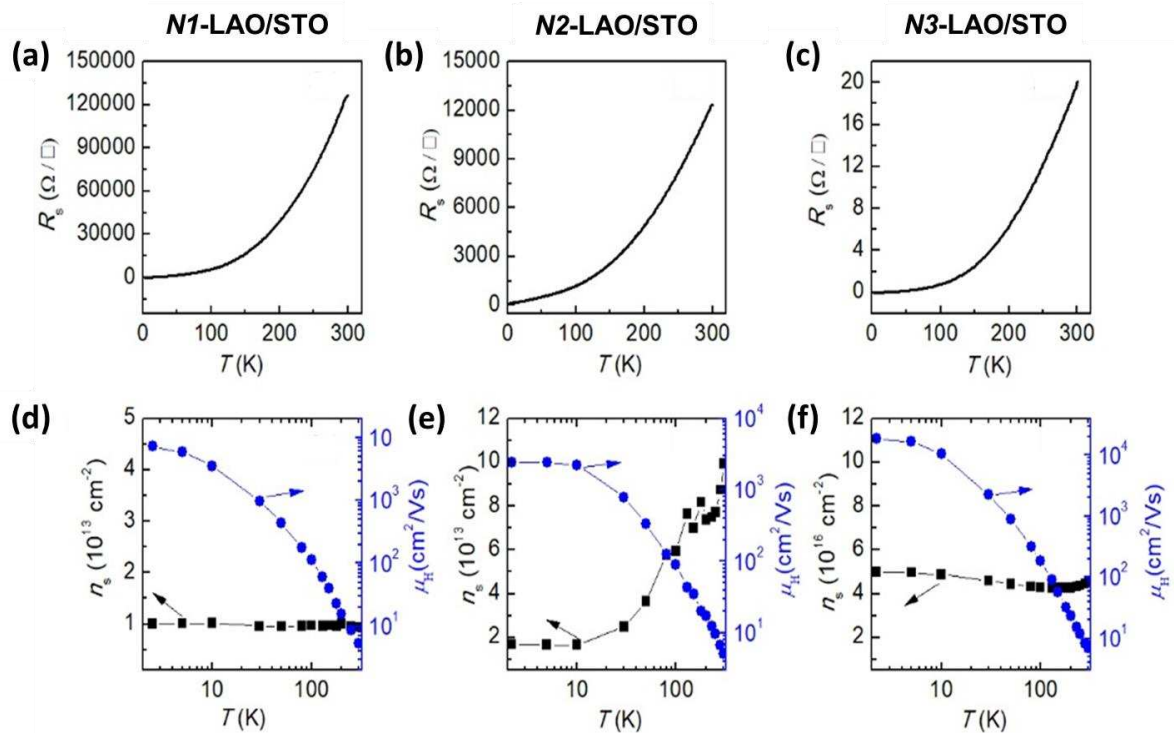**FIG. S1.** Atomic Force Microscopic image of the STO substrate after treatment.

FIG. S2. The sheet resistance, R_s versus temperature, T, for the respective LAO/STO interfaces. (a) *N1*-LAO/STO, (b) *N2*-LAO/STO, and (c) *N3*-LAO/STO. The carrier density n_s, and Hall mobility μ_H, as a function of T for LAO/STO interfaces. (d) *N1*-LAO/STO, (e) *N2*-LAO/STO, and (f) *N3*-LAO/STO.
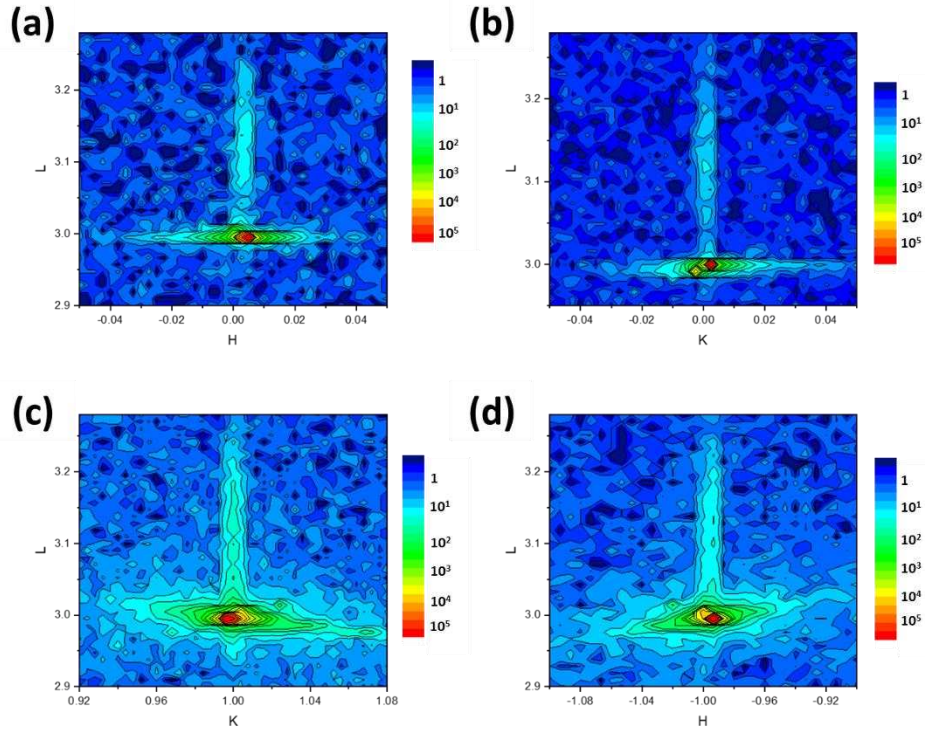
FIG. S3. X-ray Diffraction measurements. Reciprocal space mapping (RSM). (a) $(003)_{HL}$, (b) $(003)_{KL}$, (c) $(013)_{KL}$ and, (d) $(-103)_{HL}$ for *N1*-LAO/STO.
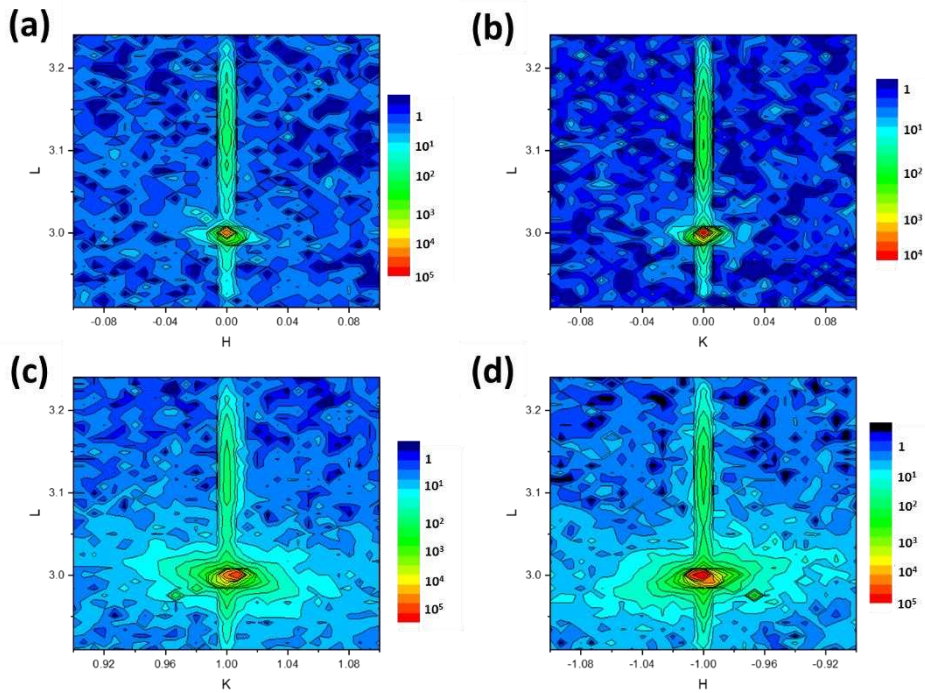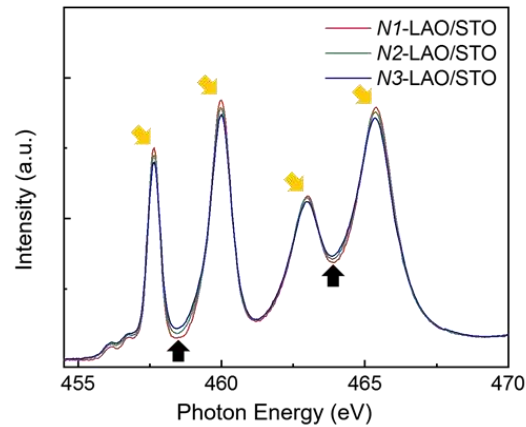

FIG. S4. X-ray Diffraction measurements. Reciprocal space mapping (RSM). (a) $(003)_{HL}$, (b) $(003)_{KL}$, (c) $(013)_{KL}$ and, (d) $(-103)_{HL}$ for *N2*-LAO/STO.
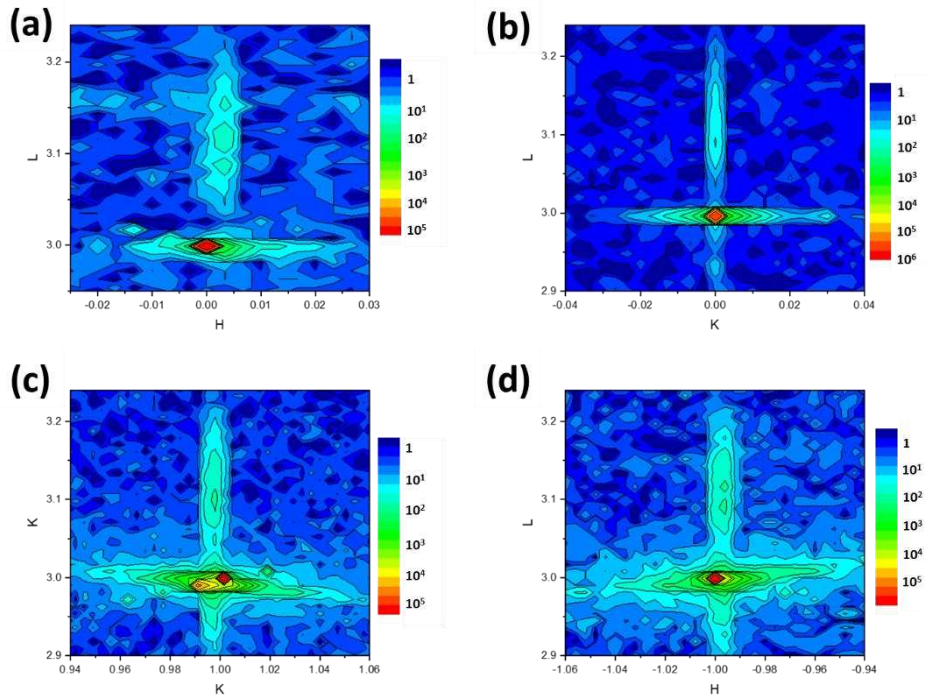
FIG. S5. X-ray Diffraction measurements. Reciprocal space mapping (RSM). (a) $(003)_{HL}$, (b) $(003)_{KL}$, (c) $(013)_{KL}$ and, (d) $(-103)_{HL}$ for *N3*-LAO/STO.

FIG. S6. Characterizing Ti valence state for the LAO/STO interfaces based on Ti L-edge XAS characterization. Yellow arrows denote the positions of the characteristic L-edge peaks corresponding to the Ti^{4+} states while black arrows denote those of the corresponding Ti^{3+} states.
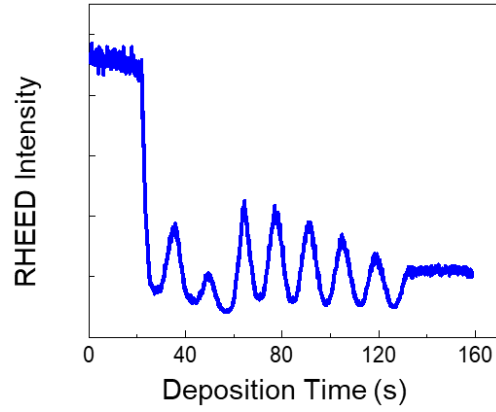
FIG. S7. Growth of crystalline 8 uc *N1*-LAO/STO *in-situ* monitored using reflection high-energy electron diffraction (RHEED).
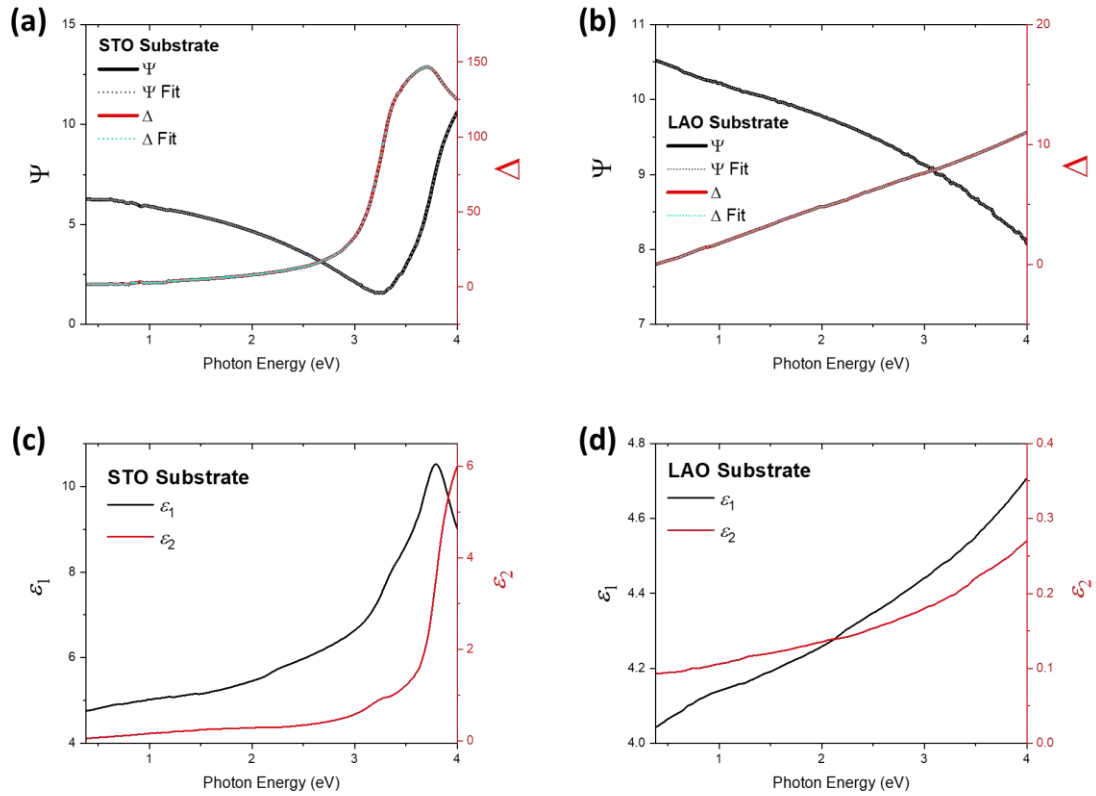

FIG. S8. (a) Raw optical data Ψ and Δ belonging to the STO substrate measured at room temperature at incident angle 70° overlayed with the experimental fitting with surface roughness taken into consideration (see dotting points), and (c) its eventual elucidated ε_1 and ε_2 spectra. (b) Raw optical data Ψ and Δ belonging to the LAO substrate measured at room temperature at incident angle 70° overlayed with the experimental fitting with surface roughness taken into consideration (see dotting points), and (d) its eventual elucidated ε_1 and ε_2 spectra.
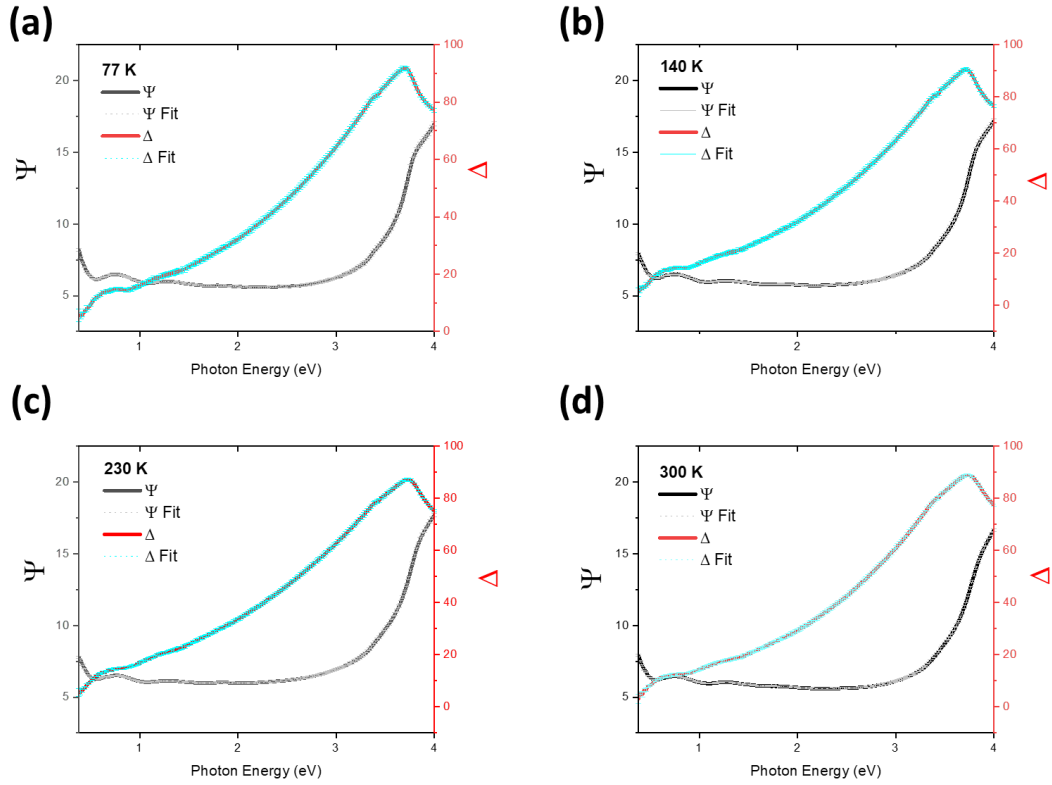
FIG. S9. Raw Ψ and Δ Data of N1-LAO/STO and their respective fit at (a) 77 K, (b) 140 K, (c) 230 K, and (d) 300 K.
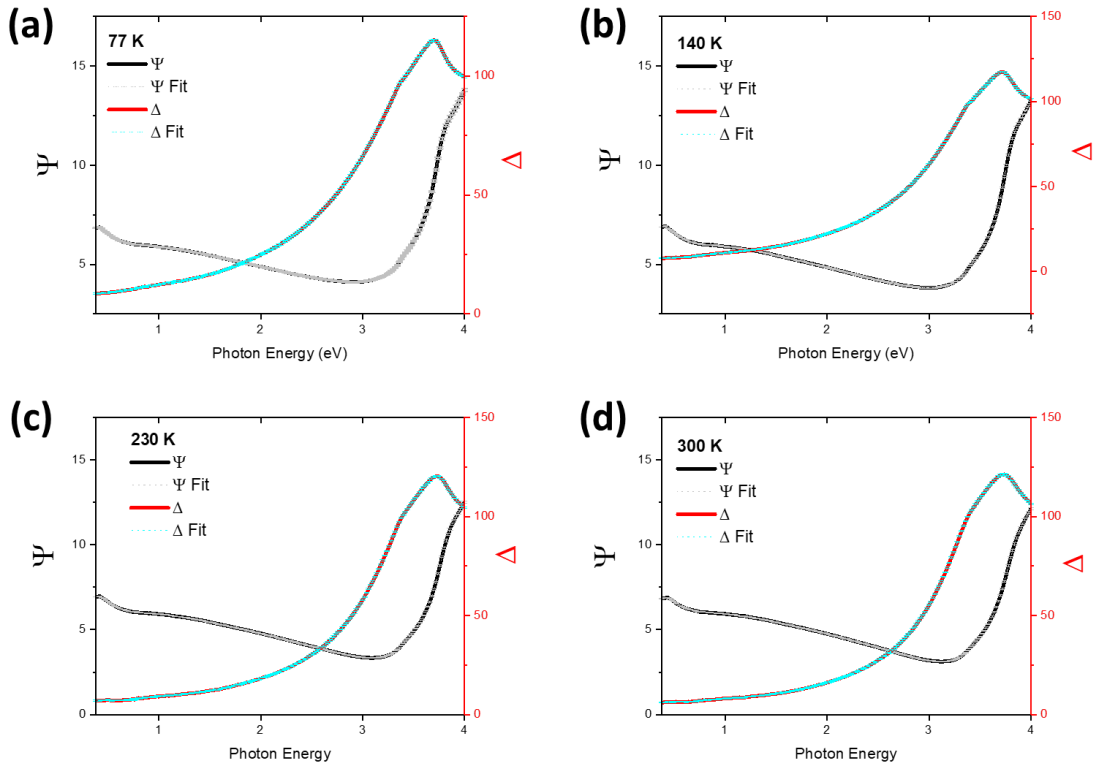

FIG. S10. Raw Ψ and Δ Data of N2-LAO/STO and their respective fit at (a) 77 K, (b) 140 K, (c) 230 K, and (d) 300 K.
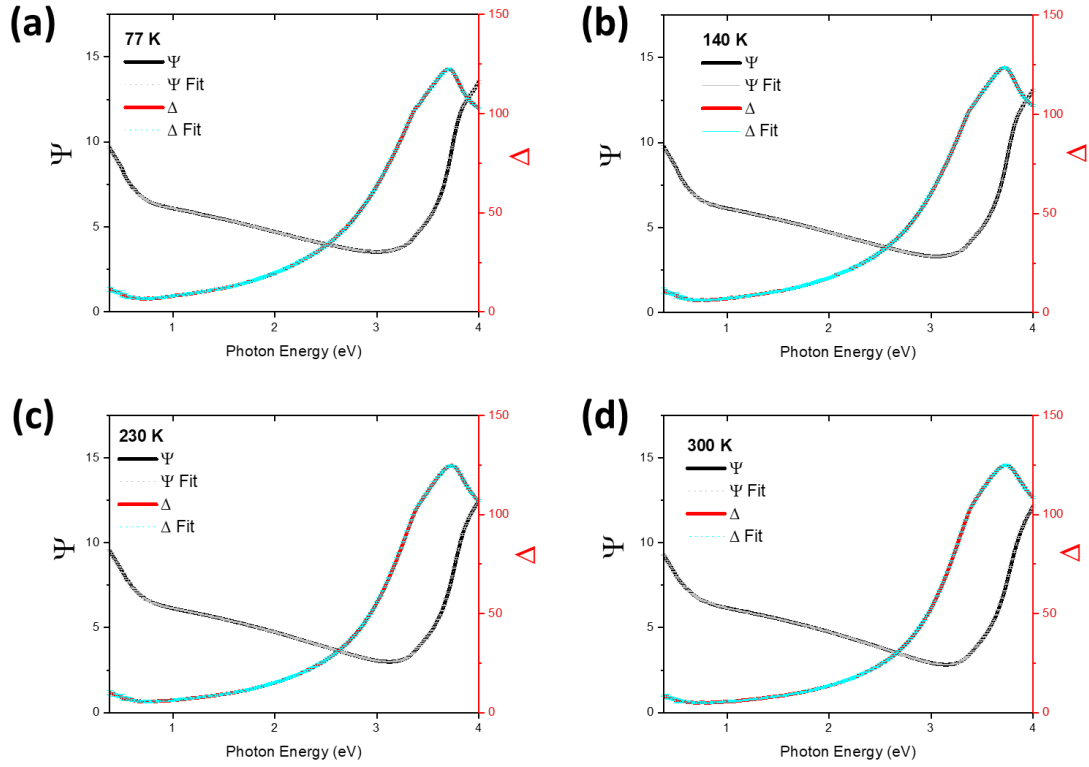
FIG. S11. Raw Ψ and Δ Data of N3-LAO/STO and their respective fit at (a) 77 K, (b) 140 K, (c) 230 K, and (d) 300 K.
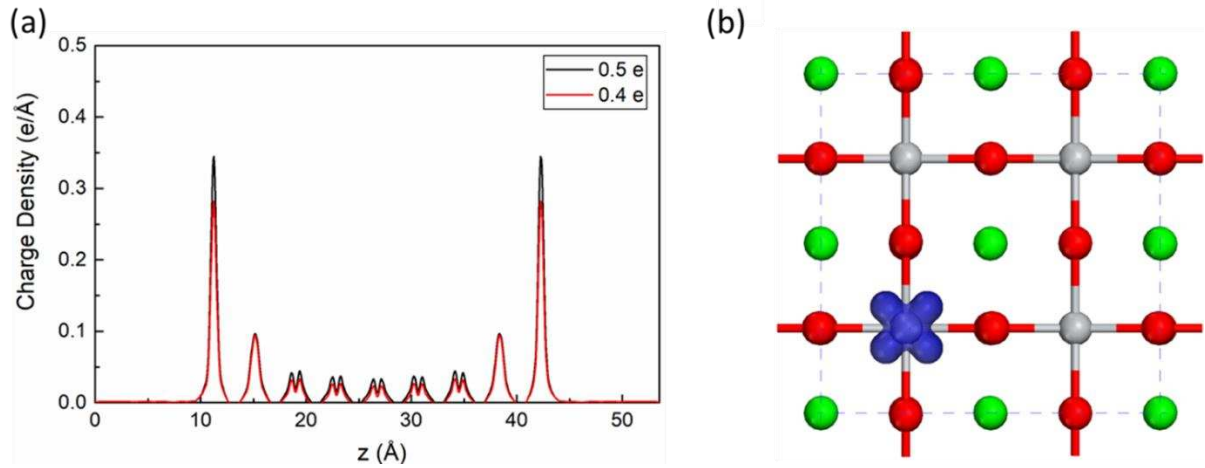

FIG. S12. PDOS study of the LAO/STO interfacial small polaron. (a) The in-plane averaged partial charge density of more conducting (0.5 e/u.c. – in red) and less conducting (0.4 e/u.c. – in black) at the LAO/STO interface. (b) Top view of the visualized polaron state in the more conducting LAO/STO interface with an iso-surface value of 1.5×10^{-3} e/Å^3.
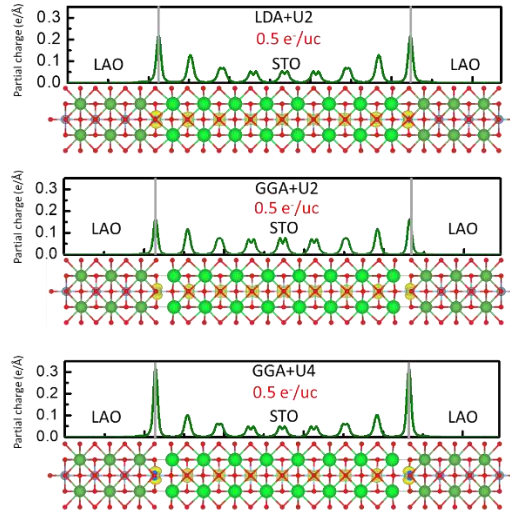
FIG. S13. The effect of exchange-functionals and Hubbard U values on the charge-transfer and carrier density distribution at the LAO/STO interface where the charge-transfer remains at 0.5e$^-$/uc despite different Hubbard U.
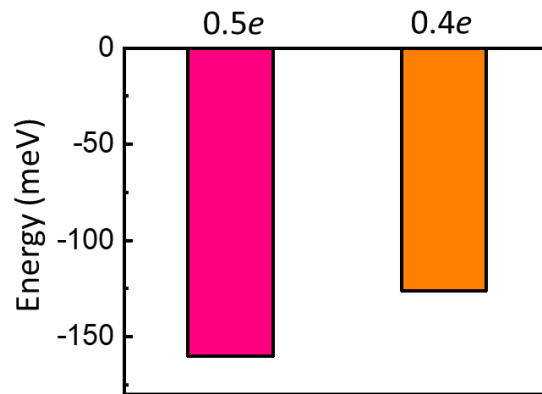

FIG. S14. Comparing the formation energy of small polarons for at an interfacial electron density of 0.5e and 0.4e at the interfacial TiO_2 sublayer.

VIII. REFERENCES

1.   Ariando, X. Wang, G. Baskaran, Z. Q. Liu, J. Huijben, J. B. Yi, A. Annadi, A. R. Barman, A. Rusydi, S. Dhar, Y. P. Feng, J. Ding, H. Hilgenkamp and T. Venkatesan, Nature Communications **2** (1), 188 (2011).

2.   S. W. Zeng, X. M. Yin, T. S. Herng, K. Han, Z. Huang, L. C. Zhang, C. J. Li, W. X. Zhou, D. Y. Wan, P. Yang, J. Ding, A. T. S. Wee, J. M. D. Coey, T. Venkatesan, A. Rusydi and A. Ariando, Physical Review Letters **121** (14), 146802 (2018).

3.   J. S. Lee, Y. W. Xie, H. K. Sato, C. Bell, Y. Hikita, H. Y. Hwang and C. C. Kao, Nature Materials **12** (8), 703-706 (2013).

4.   X. Yin, M. Yang, C. S. Tang, Q. Wang, L. Xu, J. Wu, P. E. Trevisanutto, S. Zeng, X. Y. Chin, T. C. Asmara, Y. P. Feng, A. Ariando, M. Chhowalla, S. J. Wang, W. Zhang, A. Rusydi and A. T. S. Wee, Advanced Science **6** (12), 1900446 (2019).

5.   T. C. Asmara, I. Santoso and A. Rusydi, Review of Scientific Instruments **85** (12), 123116 (2014).

6.   M. Basletic, J. L. Maurice, C. Carrétéro, G. Herranz, O. Copie, M. Bibes, É. Jacquet, K. Bouzehouane, S. Fusil and A. Barthélémy, Nature Materials **7** (8), 621-625 (2008).

7.   K. Janicka, J. P. Velev and E. Y. Tsymbal, Physical Review Letters **102** (10), 106803 (2009).

8.   W.-j. Son, E. Cho, B. Lee, J. Lee and S. Han, Physical Review B **79** (24), 245411 (2009).

9.   A. Dubroka, M. Rössle, K. W. Kim, V. K. Malik, L. Schultz, S. Thiel, C. W. Schneider, J. Mannhart, G. Herranz, O. Copie, M. Bibes, A. Barthélémy and C. Bernhard, Physical Review Letters **104** (15), 156807 (2010).

10.   N. Reyren, S. Thiel, A. D. Caviglia, L. F. Kourkoutis, G. Hammerl, C. Richter, C. W. Schneider, T. Kopp, A. S. Rüetschi, D. Jaccard, M. Gabay, D. A. Muller, J. M. Triscone and J. Mannhart, Science **317** (5842), 1196-1199 (2007).

11.   W. Siemons, G. Koster, H. Yamamoto, W. A. Harrison, G. Lucovsky, T. H. Geballe, D. H. A. Blank and M. R. Beasley, Physical Review Letters **98** (19), 196802 (2007).

12.   M. Sing, G. Berner, K. Goß, A. Müller, A. Ruff, A. Wetscherek, S. Thiel, J. Mannhart, S. A. Pauli, C. W. Schneider, P. R. Willmott, M. Gorgoi, F. Schäfers and R. Claessen, Physical Review Letters **102** (17), 176805 (2009).

13.   T. C. Asmara, A. Annadi, I. Santoso, P. K. Gogoi, A. Kotlov, H. M. Omer, M. Motapothula, M. B. H. Breese, M. Rübhausen, T. Venkatesan, Ariando and A. Rusydi, Nature Communications **5** (1), 3663 (2014).

14.   C. A. Triana, C. G. Granqvist and G. A. Niklasson, Journal of Applied Physics **118** (2), 024901 (2015).

15.   C. A. Triana, C. G. Granqvist and G. A. Niklasson, Journal of Applied Physics **119** (1), 015701 (2016).

16.   V. V. Bryksin, Fiz. Tverd. Tela (Leningrad) **24**, 1110 (1982).

17.   D. Emin, Physical Review B **48** (18), 13691-13702 (1993).

18.   B. V. V, Sov. Phys. Solid State **24** (627) (1982).

19.   C. Cancellieri, A. S. Mishchenko, U. Aschauer, A. Filippetti, C. Faber, O. S. Barišić, V. A. Rogalev, T. Schmitt, N. Nagaosa and V. N. Strocov, Nature Communications **7** (1), 10386 (2016).

20.   A. S. Alexandrov and J. T. Devreese, *Advances in Polaron Physics*. (Springer Berlin Heidelberg, Berlin, Heidelberg, 2010).

21.   *Polarons in Advanced Materials*, 1 ed. (Springer Netherlands, Dordrecht, 2007).

22.   J. L. M. van Mechelen, D. van der Marel, C. Grimaldi, A. B. Kuzmenko, N. P. Armitage, N. Reyren, H. Hagemann and I. I. Mazin, Physical Review Letters **100** (22), 226403 (2008).

23.   W. Meevasana, X. J. Zhou, B. Moritz, C. C. Chen, R. H. He, S. I. Fujimori, D. H. Lu, S. K. Mo, R. G. Moore, F. Baumberger, T. P. Devereaux, D. van der Marel, N. Nagaosa, J. Zaanen and Z. X. Shen, New Journal of Physics **12** (2), 023004 (2010).

24.   C. L. Jia, S. B. Mi, M. Faley, U. Poppe, J. Schubert and K. Urban, Physical Review B **79** (8), 081405 (2009).

25.   D. Doennig and R. Pentcheva, Scientific Reports **5** (1), 7909 (2015).
26.   G. Verbist, F. M. Peeters and J. T. Devreese, Ferroelectrics **130** (1), 27-34 (1992).
27.   F. Cadiz, E. Courtade, C. Robert, G. Wang, Y. Shen, H. Cai, T. Taniguchi, K. Watanabe, H. Carrere, D. Lagarde, M. Manca, T. Amand, P. Renucci, S. Tongay, X. Marie and B. Urbaszek, Physical Review X **7** (2), 021026 (2017).
28.   K. He, N. Kumar, L. Zhao, Z. Wang, K. F. Mak, H. Zhao and J. Shan, Physical Review Letters **113** (2), 026803 (2014).
29.   A. Fête, S. Gariglio, C. Berthod, D. Li, D. Stornaiuolo, M. Gabay and J. M. Triscone, New Journal of Physics **16** (11), 112002 (2014).
30.   D. Pines, Reviews of Modern Physics **28** (3), 184-198 (1956).
31.   X. Yin, C. S. Tang, S. Zeng, T. C. Asmara, P. Yang, M. A. Naradipa, P. E. Trevisanutto, T. Shirakawa, B. H. Kim, S. Yunoki, M. B. H. Breese, T. Venkatesan, A. T. S. Wee, A. Ariando and A. Rusydi, ACS Photonics **6** (12), 3281-3289 (2019).
32.   G. Kresse and J. Hafner, Physical Review B **47** (1), 558-561 (1993).
33.   G. Kresse and J. Hafner, Physical Review B **48** (17), 13115-13118 (1993).
34.   G. Kresse and D. Joubert, Physical Review B **59** (3), 1758-1775 (1999).
35.   A. I. Liechtenstein, V. I. Anisimov and J. Zaanen, Physical Review B **52** (8), R5467-R5470 (1995).
36.   A. Ohtomo and H. Y. Hwang, Nature **427** (6973), 423-426 (2004).
37.   M. Behtash, S. Nazir, Y. Wang and K. Yang, Physical Chemistry Chemical Physics **18** (9), 6831-6838 (2016).
38.   Z. S. Popović, S. Satpathy and R. M. Martin, Physical Review Letters **101** (25), 256801 (2008).
39.   M. Stengel and D. Vanderbilt, Physical Review B **80** (24), 241103 (2009).
40.   I. V. Maznichenko, S. Ostanin, A. Ernst, J. Henk and I. Mertig, physica status solidi (b) **257** (7), 1900540 (2020).
41.   S. Okamoto, A. J. Millis and N. A. Spaldin, Physical Review Letters **97** (5), 056802 (2006).
42.   Z. Wang and K. H. Bevan, Physical Review B **93** (2), 024303 (2016).
43.   S. Chrétien and H. Metiu, The Journal of Physical Chemistry C **115** (11), 4696-4705 (2011).
44.   T. Shibuya, K. Yasuoka, S. Mirbt and B. Sanyal, Journal of Physics: Condensed Matter **24** (43), 435504 (2012).
45.   A. Chaudhuri, L. Mandal, X. Chi, M. Yang, M. C. Scott, M. Motapothula, X. J. Yu, P. Yang, Y. Shao-Horn, T. Venkatesan, A. T. S. Wee and A. Rusydi, Physical Review B **97** (19), 195150 (2018).
46.   M. Setvin, C. Franchini, X. Hao, M. Schmid, A. Janotti, M. Kaltak, C. G. Van de Walle, G. Kresse and U. Diebold, Physical Review Letters **113** (8), 086402 (2014).
47.   M. Reticcioli, M. Setvin, M. Schmid, U. Diebold and C. Franchini, Physical Review B **98** (4), 045306 (2018).
48.   Y. Cao, V. Fatemi, S. Fang, K. Watanabe, T. Taniguchi, E. Kaxiras and P. Jarillo-Herrero, Nature **556** (7699), 43-50 (2018).
49.   X. Lu, P. Stepanov, W. Yang, M. Xie, M. A. Aamir, I. Das, C. Urgell, K. Watanabe, T. Taniguchi, G. Zhang, A. Bachtold, A. H. MacDonald and D. K. Efetov, Nature **574** (7780), 653-657 (2019).
50.   C. Franchini, M. Reticcioli, M. Setvin and U. Diebold, Nature Reviews Materials **6** (7), 560-586 (2021).
51.   S. Zhang, in *Handbook of Materials Modeling : Methods: Theory and Modeling*, edited by W. Andreoni and S. Yip (Springer International Publishing, Cham, 2018), pp. 1-27.
52.   S. Gariglio, N. Reyren, A. D. Caviglia and J. M. Triscone, Journal of Physics: Condensed Matter **21** (16), 164213 (2009).
53.   H. Y. Hwang, Y. Iwasa, M. Kawasaki, B. Keimer, N. Nagaosa and Y. Tokura, Nature Materials **11** (2), 103-113 (2012).
54.   G. Swartz Adrian, H. Inoue, A. Merz Tyler, Y. Hikita, S. Raghu, P. Devereaux Thomas, S. Johnston and Y. Hwang Harold, Proceedings of the National Academy of Sciences **115** (7), 1475-1480 (2018).

55.   S. Zhang, T. Wei, J. Guan, Q. Zhu, W. Qin, W. Wang, J. Zhang, E. W. Plummer, X. Zhu, Z. Zhang and J. Guo, Physical Review Letters **122** (6), 066802 (2019).

56.   Y. Cao, V. Fatemi, A. Demir, S. Fang, S. L. Tomarken, J. Y. Luo, J. D. Sanchez-Yamagishi, K. Watanabe, T. Taniguchi, E. Kaxiras, R. C. Ashoori and P. Jarillo-Herrero, Nature **556** (7699), 80-84 (2018).

57.   R. Bistritzer and H. MacDonald Allan, Proceedings of the National Academy of Sciences **108** (30), 12233-12237 (2011).

58.   K. Uchida, S. Furuya, J.-I. Iwata and A. Oshiyama, Physical Review B **90** (15), 155451 (2014).

59.   E. Suárez Morell, J. D. Correa, P. Vargas, M. Pacheco and Z. Barticevic, Physical Review B **82** (12), 121407 (2010).

60.   Y. Xie, B. Lian, B. Jäck, X. Liu, C.-L. Chiu, K. Watanabe, T. Taniguchi, B. A. Bernevig and A. Yazdani, Nature **572** (7767), 101-105 (2019).